

Title: Dynamics of the IFT Machinery at the Ciliary Tip

Alexander Chien^{1*} and Sheng Min Shih^{2*}, Raqual Bower³, Douglas Tritschler³, Mary E. Porter³, Ahmet Yildiz^{1,2,4}

¹Biophysics Graduate Group, ²Physics Department, and ⁴Department of Molecular and Cell Biology, University of California, Berkeley, Berkeley, CA, 94720. ³Department of Genetics, Cell Biology, and Development, University of Minnesota, Minneapolis, MN 55455

*These authors contributed equally to this work.

Correspondence and requests for materials should be addressed to A.Y. (email: yildiz@berkeley.edu).

10 **Abstract:**

11 Intraflagellar transport (IFT) is essential for the elongation and maintenance of eukaryotic cilia
12 and flagella. Due to the traffic jam of multiple trains at the ciliary tip, how IFT trains are
13 remodeled in these turnaround zones cannot be determined by conventional imaging. Using
14 Photogate, we visualized the full range of movement of single IFT trains and motors
15 in *Chlamydomonas* flagella. Anterograde trains split apart and IFT complexes mix with each
16 other at the tip to assemble retrograde trains. Dynein-1b is carried to the tip by kinesin-II as
17 inactive cargo on anterograde trains. Unlike dynein-1b, kinesin-II detaches from IFT trains at the
18 tip and diffuses in flagella. As the flagellum grows longer, diffusion delays return of kinesin-II to
19 the basal body, depleting kinesin-II available for anterograde transport. Our results suggest that
20 dissociation of kinesin-II from IFT trains serves as a negative feedback mechanism that
21 facilitates flagellar length control in *Chlamydomonas*.

Introduction

Cilia (or eukaryotic flagella, terms essentially referring to the same organelle) are hair-like organelles that extend from the plasma membrane of nearly all mammalian cells. The core structural component of a cilium is the axoneme, a ring of nine unipolar doublet microtubules surrounding a central pair of singlet microtubules. Cilia play essential roles in cell motility, generate the movement of fluids over multiciliated surfaces, and sense extracellular signals (Satir et al., 2010). To assemble and maintain functional cilia, the IFT machinery (Kozminski et al., 1993) transports axonemal precursors and sensory proteins bidirectionally between the cell body and the ciliary tip. Defects in IFT are linked to a wide range of human diseases including Bardet-Biedl syndrome, retinal degeneration, and polycystic kidney disease (Brown and Witman, 2014).

Intraflagellar cargoes interact with multiprotein complexes known as IFT particles that are organized into larger IFT trains as they enter the flagellum (Cole et al., 1998; Lechtreck et al., 2017; Pigino et al., 2009). In most species, the IFT trains are transported anterogradely from the base to the tip of a flagellum by heterotrimeric kinesin-II (Kozminski et al., 1995), but some species also use a second homodimeric kinesin to build more specialized sensory cilia (Snow et al., 2004). Once the trains reach the tip, they are reorganized and transported retrogradely to the ciliary base by dynein-1b (Pazour et al., 1999; Porter et al., 1999; Signor et al., 1999). Along the length of a cilium, the activities of kinesin and dynein motors are reciprocally coordinated, such that only one type of a motor is active at a time (Shih et al., 2013). As a result, trains move between the tip and base of the cilium without significant pauses or back-and-forth motion (Dentler, 2005; Engel et al., 2009) and switch directions at the turnaround zones (Ishikawa and Marshall, 2011; Laib et al., 2009; Shih et al., 2013). Dynein-1b requires kinesin-II activity to reach the ciliary tip, suggesting that it travels as an inactive passenger on anterograde trains

(Iomini et al., 2001; Pedersen et al., 2006; Rompolas et al., 2007). Because anterograde and retrograde IFT trains have different sizes and depart at different frequencies (Dentler, 2005; Iomini et al., 2001), IFT trains must be remodeled at the distal tip and the flagellar base.

The mechanism underlying the remodeling of IFT complexes at the ciliary tip and base cannot be directly observed by conventional microscopy methods because multiple trains coexist in these turnaround zones (Buisson et al., 2013; Iomini et al., 2001; Wren et al., 2013). In this work, we adapted PhotoGate (Belyy et al., 2017) to control the number of fluorescent IFT trains entering the flagellum of the unicellular algae *Chlamydomonas reinhardtii*. Using this approach, we monitored the turnaround behavior and remodeling of single IFT trains at the flagellar tip. We also elucidated the mechanisms by which the kinesin and dynein motors are recycled in this process and IFT trains reverse their direction of motion. The dynamics of IFT motor turnover at the tip suggest a new mechanism for how *Chlamydomonas* controls the length of its flagella at steady state.

Results

IFT trains split apart and mix with each other at the flagellar tip

To monitor IFT movement, we tracked the dynamic behavior of IFT27, a core component of the IFT complex B, in a *pf18 IFT27-GFP* strain (Engel et al., 2009; Qin et al., 2007). This strain has paralyzed flagella (*pf*) that readily adhere to the glass surface, enabling us to monitor IFT under total internal reflection (TIR) illumination (Engel et al., 2009). Consistent with previous studies (Dentler, 2005; Engel et al., 2009; Iomini et al., 2001; Kozminski et al., 1993; Qin et al., 2007; Shih et al., 2013), IFT trains moved processively along the length of flagella, reversing direction at the flagellar tip and base (Figure 1a, Video 1). Pausing and reversals of anterograde trains before reaching the tip were very rare. The velocity of IFT27-GFP was $2.1 \pm 0.4 \mu\text{m s}^{-1}$ in the

68 anterograde direction and $3.0 \pm 0.7 \mu\text{m s}^{-1}$ in the retrograde direction (Figure 1-figure
69 supplement 1, mean \pm s.d., $N = 80$ trains in each direction). Because a large number of GFP-
70 labeled trains accumulated at the tip, the dwell and departure of individual trains at the tip could
71 not be resolved by conventional TIR imaging (Figure 1a).

72 To monitor the turnaround behavior of individual IFT trains at the flagellar tip, we developed the
73 one-dimensional PhotoGate assay (Belyy et al., 2017) to track single fluorescent complexes at
74 the flagellar tip. In this assay, fluorescent trains located at distal parts of a flagellum were
75 initially photobleached by moving a focused laser beam from the tip of the flagellum to near its
76 base. We next opened the “gate” by turning off the focused beam until a single fluorescent train
77 entered the flagellum. The gate beam was repeatedly turned on for 0.2 s at 1 Hz to photobleach
78 any additional anterograde trains entering the flagellum (Figure 1b, Video 2). Under these
79 conditions, less than 1% of anterograde IFT trains were able to pass the gate unbleached. This
80 approach revealed the full range of movement of single fluorescent IFT trains within the
81 flagellum. IFT movement can be divided into three stages: anterograde movement toward the tip,
82 pausing at the tip, and returning to the base by retrograde transport.

83 We directly observed that a single anterograde train splits into multiple retrograde trains at the tip
84 (Figure 1c-e, Figure 1-figure supplement 2a). On average, 2.4 retrograde trains were detected
85 departing from the tip after the arrival of a single fluorescent anterograde train (Figure 1f, $N =$
86 97), consistent with higher frequencies of retrograde IFT trains than anterograde IFT trains
87 (Dentler, 2005; Iomini et al., 2001; Qin et al., 2007). However, the number of retrograde trains
88 per fluorescent anterograde train in PhotoGate assays (2.4, Figure 1c) was significantly higher
89 (Welch’s t-test, $p = 10^{-20}$) than the ratios of retrograde to anterograde train frequencies (1.15,
90 Figure 1a) (Dentler, 2005; Iomini et al., 2001; Reck et al., 2016). These observations suggested

that IFT complexes from different anterograde trains recombine with each other to form retrograde trains at the tip. To test this possibility, we closed the gate after two or three fluorescent anterograde trains entered the flagellum (Figure 1d,e, Videos 3 and 4) and measured the number and return frequency of retrograde trains departing from the tip. If individual trains split and return without mixing with each other, the number and frequency of fluorescent retrograde trains would be proportional to the number of fluorescent anterograde trains. In contrast, we observed 2.4, 3.6, and 4.2 returning trains on average for one, two, and three incoming trains, respectively ($N = 97, 60, 42$, Figure 1f). The return frequencies for one, two, and three incoming fluorescent trains were $0.57, 0.71$, and 0.76 s^{-1} , respectively. Because the increase was sub-proportional with the number of anterograde trains, we concluded that the fluorescent complexes in the anterograde trains disassemble and mix with a pool of “dark” complexes from the other photobleached trains at the tip before they reorganize into retrograde trains (Figure 1f). Monte Carlo simulations revealed that our conclusions are not markedly affected by the limited number of IFT27-GFPs per anterograde train (~ 6) or GFP photobleaching under TIR illumination (0.07 s^{-1} , Figure 1g, Figure 1-figure supplement 3, see Materials and Methods).

IFT tip turnaround is regulated by dynein activity and extracellular Ca^{2+}

To understand processing of IFT trains at the tip, we analyzed the time between the arrival of an anterograde train and the departure of fluorescent retrograde trains (referred to as tip resting time) at the tip (Figure 2a). When only a single fluorescent anterograde IFT27-GFP train was left unbleached near the base of the flagellum, the tip resting time of the 1st retrograde train was $3.1 \pm 0.3 \text{ s}$ (mean \pm s.e.m., $N = 97$, Figure 2b), comparable to that of IFT cargos (Craft et al., 2015; Reck et al., 2016; Wren et al., 2013). Tip resting time was independent of flagellar length (Figure

2-figure supplement 1). If IFT tip turnaround was rate-limited by a single process, we would expect a single exponential distribution of tip resting times. However, the tip resting time histogram of 1st retrograde trains fit well to a Gamma distribution with a shape parameter of 3 and a rate constant of $\sim 1 \text{ s}^{-1}$, indicating that tip turnaround of IFT trains occurs rapidly through a multistep process (Figure 2b). We also observed that the tip resting time of 1st, 2nd, 3rd, and 4th fluorescent retrograde trains increases linearly (Figure 2c). Because the average time between successive retrograde trains ($\Delta t = 1.7 \text{ s}$) is the same, we concluded that the tip departure is a purely stochastic process. The linear fit to the tip resting times has a y-intercept of 1.3 s (Figure 2c), revealing that the departure of the 1st train takes longer than Δt . Therefore, the complexes dwell at the tip through another rate limiting process before they can depart from the tip.

When two or three fluorescent anterograde trains were allowed to pass through the gate, Δt became shorter (1.4 and 1.3 s, Welch's t-test, $p = 0.03$ and 0.02 for two and three trains, respectively; Figure 2c). This is because providing a higher number of fluorescent GFPs available at the tip increases the likelihood of retrograde trains to have at least one fluorescent GFP. Remarkably, the y-intercept remained constant when we allowed one to three more fluorescent anterograde trains to enter the flagellum (Figure 2c), suggesting that this duration corresponds to processing and breakdown of anterograde trains at the tip (referred to as tip remodeling time). The time between tip remodeling and departure of IFT trains is defined as the tip departure time (Figure 2a).

We also tested whether extracellular calcium and the dynein inhibitor ciliobrevin D (Firestone et al., 2012) affect the duration of IFT tip turnaround. Calcium regulates pausing of IFT trains along the flagellum (Collingridge et al., 2013; Shih et al., 2013), and disrupting calcium-dependent kinesin-II phosphorylation causes abnormal accumulations of IFT proteins at the ciliary tip

(Liang et al., 2014). When extracellular calcium in media (0.34 mM) was chelated using 0.5 mM EGTA, the tip departure time increased to 2.8 s (Welch's t-test, $p = 0.01$), whereas tip remodeling time (1.4 s) remained unaltered (Figure 2d,e). Therefore, calcium has minimal effect on the breakdown of anterograde trains, but may have a regulatory role in the assembly or departure of retrograde trains. Addition of 0.1 mM ciliobrevin D to media results in 50% reduction in the frequency of retrograde and anterograde trains, and 50% and 28% reduction in retrograde and anterograde train velocities, respectively (Shih et al., 2013). In this case, the tip resting time of IFT27 increased over two-fold (Figure 2e, $p < 10^{-4}$), suggesting that rapid turnover of IFT trains depends on dynein activity.

Kinesin-II dissociates from IFT trains at the tip

We next turned our attention to the movement of the IFT motors and their exchange at the flagellar tip. Dynein-1b was tagged with GFP at its light intermediate chain (D1bLIC), which assembles into the dynein-1b complex and rescues *d1blic* mutant phenotypes (Reck et al., 2016). In the *d1blic::D1bLIC-GFP* strain, D1bLIC moved continuously in the anterograde and retrograde directions at velocities similar to that of the IFT trains (Reck et al., 2016) (Figure 3a, Figure 1-figure supplement 1). Kinesin-II was tagged with GFP at its non-motor subunit KAP that localizes kinesin-II to the flagellar base (Mueller et al., 2005). In the *fla3::KAP-GFP* strain, KAP moved primarily in the anterograde direction to the flagellar tip at a similar speed to anterograde IFT27 (Figure 3b, Figure 1-figure supplement 1). Unlike D1bLIC, retrograde traces of KAP were not frequently observed (Engel et al., 2009; Wingfield et al., 2017), suggesting that kinesin-II dissociates from IFT trains at the tip (Engel et al., 2009, 2012).

PhotoGate assays revealed that D1bLIC-GFP has similar tip turnaround dynamics to IFT27-GFP (Figure 3c, figure 1-figure supplement 2b, Video 5). After arrival of a single anterograde

160 D1bLIC-GFP train at the tip, we detected on average 2.5 retrograde D1bLIC trains. The average
 161 tip resting time until the departure of the first retrograde train was 1.8 ± 0.2 s (mean \pm s.e.m., $N =$
 162 60, Figure 3d), with additional $\sim 1.1 \pm 0.1$ s between subsequent departure events (Figure 3e).
 163 PhotoGate imaging of KAP-GFP cells showed that single KAP-GFP trains moved anterogradely
 164 to the tip and rested at the tip for 2.2 ± 0.2 s ($N = 95$). Unlike D1bLIC, individual KAP-GFP
 165 particles moved away from the tip by rapid saltatory motion (Figure 3f,g, Figure 1-figure
 166 supplement 2c, Video 6). Mean square displacement (MSD) analysis showed that KAP
 167 undergoes one-dimensional diffusion at $1.68 \pm 0.04 \mu\text{m}^2 \text{s}^{-1}$ (mean \pm s.e.m., $N = 27$ traces) within
 168 the flagellum after it departs from the tip (Figure 3h), consistent with the values measured for
 169 tubulin and EB1 that undergo diffusion within the ciliary space (Craft et al., 2015; Harris et al.,
 170 2016). The tip resting time of KAP remained nearly constant at different steady-state flagellar
 171 lengths (Figure 2-figure supplement 1) and was shorter than that of IFT27, indicating that
 172 departure of kinesin from the tip is independent of flagellar length and departure of retrograde
 173 trains (Figure 2-figure supplement 1).

174 Unlike IFT trains, the majority (89%, $N = 95$) of KAP-GFPs simultaneously departed from the
 175 tip in a single step (Figure 3-figure supplement 1). Because each anterograde train contains
 176 multiple (6) KAP-GFPs on average (Engel et al., 2009), this observation indicates that kinesin-II
 177 departs from the tip in the same oligomeric state as it arrives. 34% of kymographs clearly
 178 showed a single diffusing fluorescent spot after departure (Figure 3f), suggesting that KAPs are
 179 held together in a single complex. In 30% of kymographs, the KAP signal spread quickly along
 180 the length of a flagellum after departure, suggesting that kinesin-IIs can also diffuse alone
 181 (Figure 3-figure supplement 2, Video 7). The rest of the kymographs were ambiguous. Similar to
 182 IFT27, the tip resting time of KAP increased $\sim 50\%$ when the cells were treated with ciliobrevin

D ($p = 0.0016$), but EGTA had no significant effect on tip resting time of KAP (Figure 3-figure supplement 1).

We next investigated whether KAP slides linearly along the microtubule track, similar to the non-processive, microtubule-depolymerizing kinesin MCAK (Helenius et al., 2006). In this case, KAP clusters are expected to move along the microtubule long axis, so the fluctuation in KAP position in the perpendicular axis would be similar to the error of single particle tracking. The KAP-GFP particles had lateral fluctuations of 19 ± 2 nm (mean \pm s.d.) when moving in the anterograde direction. After departing from the tip, lateral fluctuations of diffusing spots increased to 65 ± 7 nm (Figure 3i,j), comparable to the radius of the axoneme. The intensity of fluorescent spots stayed relatively constant during anterograde transport and diffusion, suggesting that the measured lateral fluctuations are due to diffusive motion rather than decreased tracking precision. We concluded that after KAP detaches from the flagellar tip, it freely explores the space between the flagellar membrane and the axonemal surface rather than sliding along microtubules.

Kinesin-II carries dynein-1b as an inactive passenger during anterograde IFT

To investigate how kinesin-II and dynein-1b motors interact with anterograde and retrograde trains and how they are recycled back to the basal body, we transformed a *dlblic* mutant with both *D1bLIC-crCherry* and *KAP-GFP* constructs and simultaneously tracked the movement of KAP and D1bLIC subunits in the rescued cells (Figure 4-figure supplement 1, Video 8). The *D1bLIC-crCherry* transgene rescued the flagellar assembly defects in the *dlblic* mutant, increasing the flagellar length to 12.2 ± 1.6 μ m (mean \pm s.d., $N = 100$ flagella). Both tagged motors were expressed at near wild-type levels (Figure 4-figure supplement 1). The velocities of anterograde and retrograde D1bLIC-crCherry trains were similar to those observed with IFT27-

GFP (Figure 4a, Figure 1-figure supplement 1). We observed strong co-localization of D1bLIC-crCherry and KAP-GFP on anterograde trajectories (Figure 4a), demonstrating that dynein-1b is carried to the flagellar tip by kinesin-II. Only D1bLIC-crCherry trains showed robust retrograde transport, while retrograde traces of KAP-GFP were rarely observed, consistent with dissociation of kinesin-II from IFT trains at the tip.

To determine which motor first departs from the tip after the arrival of an anterograde train, we performed two-color Photogate experiments to simultaneously track KAP-GFP and D1bLIC-crCherry from individual anterograde trains (Figure 4b). Out of 21 cells, KAP began diffusive motion before the retrograde movement of D1bLIC in 10 cells (Figure 4b), D1bLIC left the tip before KAP in 8 cells (Figure 4-figure supplement 2), and both appeared to exit the tip simultaneously (within 0.24 s) in 3 cells. These results suggest that kinesin-II and dynein-1b exit the flagellar tip independently from each other.

Kinesin-II returns from the ciliary tip to the cell body by diffusion

Dissociation of KAP from IFT trains at the tip is consistent with the recycling of kinesin-II to the cell body in the absence of active retrograde IFT (Engel et al., 2012; Pedersen et al., 2006; Reck et al., 2016). However, it remained unclear how kinesin-II achieves this long-range movement without active transport. To test whether diffusion from the tip effectively recycles KAP to the cell body, we performed fluorescence recovery after photobleaching (FRAP) assays in the middle sections of full-length flagella of *fla3::KAP-GFP* cells (~12 μ m, Figure 5a, Video 9). Directional movements of KAP-GFP labeled trains into the photobleached area were seen from the anterograde direction, whereas recovery of GFP fluorescence from the retrograde direction was primarily due to diffusion of KAP-GFP from the tip. These results suggest that the high levels of background observed in KAP-GFP flagella were caused by kinesin-II motors

dissociated from IFT trains at the tip. The diffusion constant calculated from the fluorescence recovery ($1.8 \pm 0.1 \mu\text{m}^2 \text{s}^{-1}$, Figure 5b) was similar to the result of the MSD analysis (Figure 3h). The fluorescent background in KAP-GFP flagella increased towards the tip, suggesting a net efflux of diffusing KAP-GFP towards the cell body (Figure 5c,d). During flagellar regrowth, the KAP-GFP gradient was maintained for all flagellar lengths (Figure 5-figure supplement 1a, see Materials and Methods). The influx of KAP-GFP fluorescence to the flagellum through anterograde IFT was statistically indistinguishable from the efflux of KAP-GFP to the base through one-dimensional diffusion in flagella (Welch's t-test, $p = 0.80$, $N = 57$, Figure 5-figure supplement 2, see Materials and Methods). These results strongly indicate that KAP-GFP returns to the cell body by diffusing from the flagellar tip.

We ran Monte Carlo simulations to estimate the accumulation of KAP in a flagellum at a steady-state using the measured values of IFT train loading (Engel et al., 2009), diffusion coefficient, flagellar length, and IFT train frequency. The model assumes that KAP is released from anterograde IFT trains at the tip, diffuses within a flagellum, and is taken up by the basal body. Under these conditions, simulations confirmed the build-up of a linear concentration gradient of KAP in the flagellum (Figure 5-figure supplement 1b). In fully-grown flagella, the return of KAP to the flagellar base takes 42 s on average, an order of magnitude longer than the travel of retrograde trains (4 s) to the base. This delay leads to a ~4-fold higher amount of KAP inside the flagellum compared to a case in which KAP returns to the base with retrograde trains (Figure 5-figure supplement 1c). Unlike KAP, IFT27-GFP cells have a low fluorescence background without an obvious concentration gradient along the length of the flagellum (Figure 5d) due to active transport of the IFT trains in both directions.

Kinesin-II is depleted from the basal body during flagellar regrowth

KAP-GFP loading on IFT particles has been shown to decrease with increasing flagellar length (Engel et al., 2009), but the underlying mechanism remained unclear. Because a larger amount of KAP builds up in the flagellum as the flagella elongate (Figure 5-figure supplement 1), loading of KAP onto the subsequent IFT trains may be reduced by depletion of KAP at the flagellar base. To test this model, we deflagellated *fla3::KAP-GFP* cells and measured the GFP fluorescence at the basal body and in the flagellum during flagellar regrowth using confocal microscopy (Figure 6a). We estimated that the total amount of KAP localized to the base and flagellum increased by two-fold with flagellar length, indicating the upregulation of IFT components during flagellar growth. The fluorescence intensity at the flagellar base was highest for short flagella (1-4 μm) and decreased ~ 4 -fold as cells grew full-length flagella ($\sim 10 \mu\text{m}$, Figure 6b), significantly larger than ~ 1.6 -fold reduction reported previously (Ludington et al., 2015). We also observed that the KAP fluorescence in the flagellum was low in short flagella and increased ~ 10 -fold as the flagellar length reached the steady-state (Figure 6b).

Changes in the amount of IFT complexes were markedly different from that of KAP during flagellar regrowth (Figure 6a). Unlike KAP-GFP, basal body fluorescence of IFT20-GFP remained nearly constant across all flagellar lengths in IFT20::IFT20-GFP cells (Figure 6c), presumably because they are rapidly returned to the base through active transport. We also observed an increase of the GFP signal in the flagellum with elongation (Figure 6c), in contrast to the previous observation that the total amount of IFT components remains constant during flagellar regeneration (Marshall and Rosenbaum, 2001). This discrepancy may be related to differences in methods for quantifying IFT components in flagella.

We next determined the localization of KAP-GFP to the basal body and flagellum in cells that grow abnormally long and short flagella. *Chlamydomonas* grows $\sim 1.5\text{X}$ longer flagella in the

presence of Li^+ (Nakamura et al., 1987) by recruiting flagellar proteins from the cell body pool into the flagella (Nakamura et al., 1987) rather than requiring new protein synthesis (Wilson and Lefebvre, 2004). Consistent with previous observations, the KAP-GFP strain grew longer flagella in 50 mM Li^+ . After reaching the steady state length, we calculated the total KAP fluorescence at the basal body and the flagellum (Figure 6d, Figure 6-figure supplement 1). In agreement with our model, we observed that KAP gets depleted at the basal body at equilibrium. The KAP fluorescence localized to a flagellum correlated strongly with flagellar length (Pearson's $R = 0.86$), similar to untreated cells. The total KAP fluorescence in the flagellum was 50% higher than untreated cells.

In the absence of new protein synthesis, *Chlamydomonas* can grow half-length flagella after deflagellation, suggesting that the cytoplasmic pool of flagellar proteins is at least one half of that localized to the flagellar compartment (Rosenbaum et al., 1969). We deflagellated KAP-GFP cells with pH shock and regrew their flagella in the presence of the protein synthesis inhibitor cycloheximide. In agreement with untreated and Li^+ treated cells, we observed that the KAP fluorescence at the flagellum correlates strongly with the flagellar length (Pearson's $R = 0.86$), whereas the KAP intensity was depleted at the basal body (Figure 6d, Figure 6-figure supplement 1). Total KAP fluorescence was one half of untreated cells, consistent with the fact that a large amount of KAP is lost during deflagellation. Therefore, over a wide range of flagellar lengths (2 – 22 μm), KAP gets depleted at the basal body when the flagella reach their equilibrium length.

Discussion

Remodeling of IFT complexes and motors at the flagellar tip in *Chlamydomonas*

297 Using PhotoGate, we have visualized the turnaround behavior of individual components of the
298 IFT machinery at the flagellar tip. We present evidence that when IFT trains arrive at the tip, the
299 complexes split apart and mix with complexes from other trains at the flagellar tip before
300 initiating retrograde transport (Figure 4c). This dynamic disassembly and reassembly process
301 may lead to differences in size, shape, and structure of anterograde and retrograde trains, as
302 previously suggested by transmission electron microscopy (Dentler, 2005; Stepanek and Pigino,
303 2016). Remarkably, remodeling of IFT trains is completed within 1.3 s, with a 1.7 s average
304 waiting time between the departures of successive trains, consistent with previously measured
305 values for IFT complex subunits, dynein-1b, and other axonemal cargoes (Craft et al., 2015; Qin
306 et al., 2007; Reck et al., 2016; Wren et al., 2013). Kinetic analysis of the tip resting time revealed
307 that disassembly of anterograde trains and reassembly of the retrograde trains is a multistep
308 process regulated by extracellular calcium and the concentration of active dynein motors.

309 Simultaneous tracking of the anterograde motor kinesin-II (with KAP-GFP) and the retrograde
310 motor dynein-1b (with D1bLIC-Cherry) has further revealed significant differences in how these
311 motors are recycled back and forth within a flagellum. Kinesin-II drives anterograde trains in a
312 highly processive fashion and then dissociates from the IFT trains when they reach at the
313 flagellar tip. KAP-GFP then returns to the flagellar base by diffusing within the flagellum,
314 similar to the diffusion of kinesin-1 in mammalian neurons (Blasius et al., 2013) and in contrast
315 to the retrograde transport of kinesin-II observed in other cilia (Signor et al., 1999; Broekhuis et
316 al., 2014; Williams et al., 2014; Prevo et al., 2015, see below). We propose that the diffusion of
317 KAP-GFP represents the movement of the entire heterotrimeric kinesin-II complex because KAP
318 and the kinesin-II motor subunits co-sediment in sucrose density gradients of purified flagella
319 extracts (Cole et al., 1998; Mueller et al., 2005) and neither KAP nor FLA10 accumulate in

flagella during inactivation of retrograde transport (Engel et al., 2012; Pedersen et al., 2006; Reck et al., 2016). In certain cases, KAP-GFP appears to diffuse in an oligomeric form. It remains to be studied what holds KAPs together and whether other components of the IFT trains diffuse with KAP clusters after splitting and mixing at the tip.

The retrograde motor dynein-1b is transported to the flagellar tip on anterograde trains (Reck et al., 2016). Because kinesin and dynein motors do not compete against each other in a tug-of-war on anterograde trains (Shih et al., 2013), we concluded that dynein-1b is carried as an inactive motor complex (Toropova et al., 2017; Zhang et al., 2017) and it actively engages with microtubules only when it reaches the flagellar tip (Figure 4c). The average tip resting time of dynein-1b is similar to kinesin-II (Welch's t test, $p = 0.05$), but the initiation of retrograde transport by dynein-1b does not require departure of kinesin-II motors from the tip, suggesting that these processes are independent from each other.

The dynamic behavior of the IFT motors in *Chlamydomonas* flagella differs from that in other cilia

Several studies have revealed differences in IFT in the cilia and flagella of different organisms (Prevo et al., 2017). First, the microtubule tracks can vary considerably. In *Chlamydomonas*, the axoneme contains nine doublet microtubules, each composed of a complete A-tubule (with 13 protofilaments) and an incomplete B-tubule (with 10 protofilaments). The B-tubule terminates before the A-tubule less than 1 μm from the flagellar tip (Ringo, 1967; Satish Tammana et al., 2013). Recent electron microscopy studies have revealed that anterograde IFT trains are transported primarily on the B-tubule, whereas retrograde IFT trains are transported on the A-tubule (Stepanek and Pigino, 2016). The pausing of IFT particles observed at the flagellar tip in *Chlamydomonas* may therefore reflect not only the time involved in the re-organization of the

IFT particles, but also the time required for switching between microtubule tracks.

In other cilia, such as *C. elegans* sensory and mammalian olfactory cilia, the proximal doublet microtubule segment is shorter, and the distal singlet MTs can vary significantly in length (~2.5 μm in *C. elegans* to >100 μm in mouse olfactory cilia). These cilia also employ two different kinesin-II motors for anterograde IFT (Prevo et al., 2015; Snow et al., 2004; Williams et al., 2014). In *C. elegans*, heterotrimeric kinesin-II is concentrated near the basal body region and transports anterograde IFT particles into the proximal doublet segment, where they are gradually handed over to a homodimeric kinesin-II, OSM-3, for transport into the distal singlet segment (Prevo et al., 2015; Snow et al., 2004). Unlike *Chlamydomonas*, both the heterotrimeric and homodimeric kinesin-II motors are recycled to the ciliary base by retrograde IFT, not by diffusion, in these and other metazoan cilia studied to date (Broekhuis et al., 2014; Mijalkovic et al., 2017; Prevo et al., 2015; Signor et al., 1999; Williams et al., 2014).

Another important difference between IFT in *Chlamydomonas* and metazoan cilia is the dynamic behavior of the motors themselves. IFT particles and motors move processively in the *Chlamydomonas* flagellum (Dentler, 2005), with little or no evidence for the frequent pausing and reversal along the axoneme previously described in *C. elegans* or mouse olfactory sensory cilia (Mijalkovic et al., 2017; Prevo et al., 2015). We also did not observe acceleration and deceleration of IFT motors near turnaround zones, nor the instantaneous (<600 ms) reversal of dynein-1b at the ciliary tip described in *C. elegans* (Mijalkovic et al., 2017; Prevo et al., 2015). The reasons for these differences in IFT dynamics and turnover remain unknown, but they may be related to the variations in ciliary structure and organization described above, differential phosphorylation of kinesin-II motors (Liang et al., 2014), posttranslational modification of the microtubule tracks (Stepanek and Pigino, 2016), and other unidentified factors. In addition, both

the frequency and speed of IFT is higher in *Chlamydomonas* (Dentler, 2005; Engel et al., 2009, 2012; Iomini et al., 2001; Reck et al., 2016; Snow et al., 2004; Williams et al., 2014; Wingfield et al., 2017) than that measured thus far in metazoan cilia (Li et al., 2015; Yi et al., 2017). This may allow *Chlamydomonas* to rapidly adjust the length of its flagella in response to internal or external stimuli, whereas most cilia in *C. elegans* sensory neurons or mammalian cells do not undergo extensive structural rearrangements once formed.

A model for flagellar length control in *Chlamydomonas*

Cilia and flagella serve as a model system to study how cells precisely control organelle size because they elongate only in one direction. According to the balance point model, flagellar length is set when flagellar assembly and disassembly rates reach equilibrium (Marshall et al., 2005). While the disassembly rate is independent of flagellar length (Kozminski et al., 1995), the assembly rate is determined by the injection of IFT trains (Marshall et al., 2005). The amount of material being transported by these trains to the tip is correlated strongly with the amount of material localized to the flagellar base (Ludington et al., 2013, 2015; Wren et al., 2013), which serves as a loading dock. Previous studies showed that IFT train size and the number of ciliary cargos per train scales inversely with flagellar length (Craft et al., 2015; Engel et al., 2009), consistent with the reduction of the assembly rate as flagella elongate (Marshall et al., 2005). However, it remained unclear which essential component of the IFT machinery limits the assembly of IFT trains at the basal body during elongation.

We propose that dissociation of kinesin-II from IFT trains serves as a negative feedback mechanism to control the assembly rate in *Chlamydomonas* (Ludington et al., 2015). Our results show that the majority of kinesin-II dissociates from IFT trains at the flagellar tip and diffuses within the flagellum. Diffusion leads to a large accumulation of kinesin-II in the flagellum as the

389 flagellum grows longer, while the amount of kinesin-II at the base decreases several-fold. As a
390 result, lower amounts of kinesin-II are available to bring new anterograde IFT trains to the
391 flagellar tip. This may lead to a reduction in the IFT train size and the rate of flagellar assembly
392 as the flagella elongate (Figure 6e,f). Indeed, a recent theoretical study demonstrated that
393 increased diffusion time of kinesin-II in longer flagella can explain the inverse relationship
394 between length and IFT motor recruitment rate (Hendel et al., 2017).

395 Consistent with this model, previous studies showed that KAP intensity at the basal body
396 correlates with KAP loading on IFT trains and the assembly rate during flagellar regeneration
397 (Ludington et al., 2013). In the temperature-sensitive mutant strain *fla10^{ts}*, inactivation of
398 kinesin-II motility ceases IFT and leads to resorption of the flagellum at a constant rate
399 (Kozminski et al., 1995; Marshall et al., 2005). At intermediate temperatures, flagellar length
400 correlates strongly with the estimated fraction of active kinesin-II motors in *fla10^{ts}* cells
401 (Marshall and Rosenbaum, 2001), indicating that the amount of active kinesin-II limits flagellar
402 growth. The experiments performed under Li⁺ and cycloheximide treatments (Figure 6d) also
403 support the idea that altering the amount of KAP available for the flagellar compartment
404 positively correlates with the flagellar length and that the equilibrium length is set when KAP
405 gets depleted below a certain threshold at the basal body. We note that the KAP intensity at the
406 flagellar base was lower (34-40%) in Li⁺ and cycloheximide treated cells than in control cells at
407 equilibrium (p < 0.0001, Figure 6d, left). Although the reason for this difference remains unclear,
408 it could be due to a reduction of KAP concentration in the cytoplasm or changes in the flagellar
409 disassembly rate under treatment (Wilson and Lefebvre, 2004).

410 Unlike kinesin-II, IFT components are rapidly recycled to the cell body by dynein-1b and the
411 amount of these components at the flagellar base remains nearly constant as the flagella elongate.

Therefore, the abundance of IFT components and dynein-1b at the flagellar base is not limiting to maintain the length, consistent with previous observations that a small amount of IFT complexes and dynein-1b is sufficient to maintain fully grown flagella (Reck et al., 2016; Wang et al., 2009).

Diffusion is also proposed to play a role in setting the length of bacterial flagella (Renault et al., 2017), long polymers made from a single protein flagellin. Similar to the flagellar length control model originally proposed for *Chlamydomonas* (Levy, 1974), flagellins are injected into the channel of the filament and they diffuse to reach the assembly site at the filament tip, generating a concentration gradient decreasing towards the tip. As the filament elongates, it grows more slowly because it takes longer for the components to reach the tip. In contrast to bacterial flagellin, structural components are carried to the tip by IFT in eukaryotic flagella. In *Chlamydomonas*, we showed that diffusion of kinesin-II from the tip sets a concentration gradient decreasing towards the basal body, and its return to the flagellar base is delayed as the flagella elongate. This delay limits the amount of kinesin-II available for building longer flagella.

Our model is challenged by studies showing that the kinesin-II mutant strains *fla10^{ts}* and *fla3* maintain nearly full-length flagella at permissive temperatures although they accumulate significantly lower amounts of kinesin-II in the flagellar compartment (Kozminski et al., 1995; Mueller et al., 2005; Pedersen et al., 2006). Remarkably, *fla3* cells exhibit slower flagellar regeneration (Mueller et al., 2005), consistent with our prediction that the lower amount of kinesin-II negatively affects the assembly rate. However, a more recent study showed that *fla10^{ts}* flagella contain wild-type levels of kinesin-II at permissive temperatures (Wang et al., 2009). Given these apparent discrepancies, more quantitative approaches will be required to address whether the amount of kinesin-II correlates with flagellar length.

According to the balance-point model, flagella that contain lower amounts of kinesin-II can still maintain nearly full-length if they also have a lower disassembly rate. The studies that reported a reduction in kinesin-II expression in *fla10^{ts}* and *fla3* cells also noted significantly reduced anterograde IFT frequency and IFT particle subunits in flagella (Mueller et al., 2005; Pedersen et al., 2006). This could negatively affect the disassembly rate because IFT is required for efficiently removing certain axonemal precursors (Qin et al., 2004) and resorbing the flagellum prior to mitosis. Indeed, flagellar resorption before mitosis occurs at a faster rate than flagellar disassembly after inactivation of IFT (Marshall et al., 2005; Pan and Snell, 2005).

The mechanisms that control the expression of IFT components after deflagellation, regulate the exchange of material between the basal body and cytoplasm, and load material onto IFT trains must also play a major role in determining the length of flagella. Several studies have shown that IFT components are upregulated and accumulate in large numbers at the flagellar base after deflagellation (Albee et al., 2013; Lefebvre and Rosenbaum, 1986; Stolc et al., 2005). Additionally, a large pool of IFT components in the cytoplasm partially exchanges with the flagellar pool (Buisson et al., 2013; Engel et al., 2009; Wingfield et al., 2017) because cells can grow half-length flagella after deflagellation under complete inhibition of protein synthesis (Rosenbaum et al., 1969). However, molecular cues that govern these processes remain poorly understood and further studies in mutant cell lines that have abnormally long (Nguyen et al., 2005; Tam et al., 2007) or short flagella may provide new insight for the mechanism of flagellar length control.

Materials and Methods

Strains and cell culture

The *pfl8 IFT27-GFP* strain was obtained from the Marshall laboratory (University of California San Francisco) after crossing the *IFT27-GFP* transgene into the *pfl8* background as previously described (Engel et al., 2009; Qin et al., 2007). The *ift20::IFT20-GFP* strain (Lechtreck et al., 2009) was obtained from the Lechtreck laboratory (University of Georgia). The *fla3::KAP-GFP* (Mueller et al., 2005) and *d1blic::D1bLIC-GFP* (Reck et al., 2016) strains are available from *Chlamydomonas* Resource Center at the University of Minnesota (RRID: [SCR 014960](#)). The *d1blic::D1bLIC-crCherry KAP-GFP* strain was generated as described below. These strains were not authenticated or tested for mycoplasma contamination. Strains were maintained on plates of TAP media containing 1% agar. For light microscopy, vegetative cells were resuspended in liquid TAP media at 22 °C for 24-48 hours and passaged to fresh liquid TAP before introduction into a flow chamber.

Isolation and characterization of the *d1blic::D1bLIC-crCherry KAP-GFP* strain.

The *D1bLIC-crCherry* construct was generated by subcloning a *Chlamydomonas* codon-optimized version of the Cherry tag into a genomic copy of the *D1bLIC* gene (Reck et al., 2016). The Cherry tag was amplified by PCR from the plasmid pBR9 mCherryCr (Rasala et al., 2013) and inserted into a unique *AscI* site located in the last exon of *D1bLIC*. The *D1bLIC-crCherry* construct was linearized with *Bam*HI and co-transformed into *d1blic* (CC-4487) with the selectable marker pSI103 and plated on TAP medium plus 10 µg/ml paromomycin. 960 transformants were picked into TAP media and screened for changes in colony morphology. 84 colonies were further examined by both phase contrast and fluorescence microscopy for rescue of flagellar assembly and expression of Cherry. Isolated flagella from four colonies were

analyzed by Western blot for the presence of full-length D1bLIC-Cherry. A single colony was selected for a second round of transformation using the *KAP-GFP* construct (Mueller et al., 2005) and the plasmid pHyg3 (Berthold et al., 2002) and selection on 10 µg/ml of hygromycin B. Two out of 96 transformants were identified as positive for both GFP and Cherry by fluorescence microscopy, and Western blots of isolated flagella confirmed the presence of both D1bLIC-Cherry and KAP-GFP in the rescued strains. Antibodies used included a rat antibody against *Chlamydomonas* KAP (Mueller et al., 2005), a mouse antibody against GFP (Covance, Inc.), a rabbit antibody against *Chlamydomonas* D1bLIC (Perrone et al., 2003), and a rabbit antibody against mCherry (Rockland Immunochemicals).

Drug treatment

0.34 mM Ca^{2+} in TAP media was depleted by adding 0.5 mM EGTA, which resulted in a free Ca^{2+} concentration of 1.5 µM. The concentration of free Ca^{2+} in the assay buffer as a function of added EGTA was calculated from the Chelator program (<http://maxchelator.stanford.edu>). For drug treatment assays, a final concentration of 100 µM ciliobrevin D was added to the TAP media, and the data was collected 5-10 minutes after the treatment.

For cycloheximide treatment, cells were deflagellated by pH shock and cycloheximide was added to a final concentration of 1.5 µg/ml immediately afterwards. Cells were allowed to regrow flagella for 2 hours before fixation and imaging. For Li^+ treatment, 50 mM LiCl was added to liquid cell suspensions, and cells were incubated for 2 hours before fixation and imaging.

Deflagellation and flagellar regrowth

For imaging the diffusion gradient in live *fla3::KAP-GFP* cells, we deflagellated cells in TAP

media using shear force by rapidly pushing them through a 20G1 $\frac{1}{2}$ syringe. Cells regenerating flagella were imaged in the following hour. For imaging the accumulation of GFP signal at the basal body region and in regenerating flagella, *fla3::KAP-GFP* and *IFT20::IFT20-GFP* cells were deflagellated with pH shock by adding 60 μ l 0.5 N acetic acid to 1 ml of cells in TAP media, waiting 45 seconds, and adding 60 μ l 0.5 N KOH. Cells were fixed 15, 30, 45, 60, and 75 minutes after pH shock. Fixation was done by pipetting 200 μ l of liquid TAP cell culture onto a poly-lysine treated coverslip for 1 minute, then gently treating the coverslip with 4% paraformaldehyde in water for 10 min. Afterwards, the coverslip was treated twice with 100% methanol chilled to -20 °C for 5 minutes. Coverslips were dipped in water to remove methanol, mounted in a flow chamber with TAP media, and then imaged immediately.

TIR microscopy

A custom-built objective-type TIR fluorescence microscope was set up using a Nikon TiE inverted microscope equipped with a perfect focusing unit, bright-field illumination, and a 100X 1.49 NA PlanApo oil immersion objective (Nikon). 488 nm and 561 nm solid state lasers (Coherent) were used for GFP and crCherry excitation, respectively. The angle of incident light was adjusted lower than the critical angle to illuminate a deeper field (~300 nm) near the coverslip surface. The fluorescent signal was recorded by an Andor iXon 512 x 512 electron-multiplied charge-coupled device (EM-CCD) camera. 1.5x extra magnification was used to obtain an effective pixel size of 106 nm. Data was collected at 10 Hz. Excitation laser beams were controlled by shutters (Uniblitz). Because the CCD image saturates under intense laser illumination of the focused gate beam, shutter timing was synchronized with the camera acquisition by a data acquisition card (NI, USB-6221) to minimize the number of saturated frames in recorded movies. For two-color imaging, GFP and crCherry fluorescence were

separated into two channels on a CCD camera using Optosplit II (Cairn). To avoid bleed-through between channels, movies were acquired using time-sharing between the 488 nm and 561 nm laser beams, synchronized with camera acquisition at 60 ms frame time. The effective pixel size was 160 nm.

PhotoGate assays

The PhotoGate system was assembled as previously described (Belyy et al., 2017). Briefly, a 488-nm laser beam was split into two paths using a half-wave plate and a polarizer beamsplitter cube. The first path was used for objective-type TIRF imaging. The second path was focused (2 MW cm^{-2}) to the image plane and steered with a fast piezo-driven mirror (S-330.8SL, Physik Instrumente). The piezo-driven mirror was mounted at a position conjugate to the back-focal plane of the objective to ensure that the tilting of the mirror resulted in pure translation of the focused beam in the image plane. The mirror provided a usable travel range of $30\text{ }\mu\text{m} \times 30\text{ }\mu\text{m}$ area at the image plane. The mirror's angle was updated via analog output channels of a data acquisition card (NI, USB-6221) and controlled by software custom-written in LabVIEW.

Flagellar orientation of surface adhered cells was visualized by TIRF imaging. Initially, the gate beam was placed at the tip of flagellum and moved along the flagellar orientation to prebleach the distal half of the flagellum. The gate beam was turned off when it was positioned near the base of the flagellum to allow a single fluorescent anterograde train to enter the flagellum. Occasionally ($<5\%$), two anterograde trains overlapped and entered the flagellum simultaneously. The gate beam was then turned on for 0.2 s of every 1 s to bleach other anterograde trains. Under these conditions, less than 1% of anterograde IFT trains moved faster than the cutoff speed ($3.0\text{ }\mu\text{m s}^{-1}$) and were able to escape the gate. Based on the size of the gate beam in the image plane, gating frequency was adjusted for each experiment to keep the escape

probability under 0.01. The trajectories of these trains can be distinguished from each other as they move at different speeds along the flagellum. The locations of flagellar tips were determined by brightfield imaging (data not shown). In two-color photogate experiments, the focused 488-nm laser beam was used to bleach both GFP and crCherry, and 488 and 561 beams were used in a time-sharing mode for TIR excitation.

FRAP assays

FRAP assays on the *fla3::KAP-GFP* strain were performed by photobleaching the center part of the flagellum (5 μm in length) for 200 ms at 25 kW cm^{-2} in the epifluorescence mode. The recovery of fluorescence signal in the bleached area was simultaneously monitored by imaging with a 100 W cm^{-2} TIRF excitation. The analysis was performed by measuring the total fluorescence intensity within the bleached area. Fluorescent signal of anterograde transport was manually excluded from the analysis. 13 different recovery traces were used in the MSD analysis. The intensity of each trace was normalized according to the initial and final intensity.

Confocal microscopy

fla3::KAP-GFP and *IFT20::IFT20-GFP* cells were fixed with paraformaldehyde at 15, 30, 45, 60, and 75 min intervals after deflagellation, as described above. The sample was imaged on a Zeiss confocal microscope using 488 nm laser excitation. Images were recorded with 560 nm z step, 63 nm pixel size, and 1.58 μs photon collection per pixel. Fluorescence in basal body and flagellum was quantified using ImageJ. The ratio of flagellar to basal-body KAP-GFP fluorescence in confocal images was similar to that of images recorded with TIR excitation, indicating that the fixation protocol did not result in the loss of diffusing KAP-GFP signal from the flagella. We confirmed that fixation did not alter the relative amount of KAP-GFP in the

568 flagellum and the base by comparing the flagellum to base fluorescence ratio in live and fixed
569 *fla3::KAP-GFP* cells.

570 **Data analysis**

571 Anterograde and retrograde trajectories were manually assigned from kymographs. After the
572 arrival of a single anterograde particle at the tip, the departure of fluorescent retrograde trains
573 was determined at single pixel and frame resolution. The tip resting time for each retrograde train
574 was defined as the duration between the arrival of the fluorescent anterograde train and the
575 departure of the retrograde train from the tip. Tip resting time histograms were constructed and
576 fitted to a Gamma function using MATLAB. The Gamma function was defined as $\Gamma(t) = t^{\alpha-1}e^{-\lambda t}$,
577 where α and λ are shape and rate parameters, respectively.

578 For single particle tracking analysis, the positions of fluorescent spots were determined by fitting
579 the PSFs to a 2D Gaussian. The positions were fitted throughout the movie except at the frames
580 when the gate beam was on or the frames in which the tracked particle overlapped with other
581 fluorophores. The intensity of the fluorescent spots was estimated by the volume of the 2D
582 Gaussian peak. In a typical assay, we adjusted excitation power to achieve 20-nm localization
583 accuracy at 10 Hz image acquisition rate. Individual GFP particles were tracked for 5 s on
584 average before photobleaching and the diffusion constant was obtained by MSD analysis of
585 individual spots. In certain kymographs, diffusion of individual KAPs within a flagellum could
586 not be resolved due to the diffraction limit.

587 To determine the distribution of the KAP-GFP background in flagella, anterograde trajectories in
588 kymographs of *fla3::KAP-GFP* cells were manually removed using custom ImageJ plugins. The
589 remaining pixels were averaged over the kymograph's time axis, giving a time-averaged plot of
590 the KAP-GFP background over the flagellum length. The cells were grouped by flagellar length.

The background intensity and flagellum length of each cell were normalized. The average background intensity along the length of the flagellum was calculated for each group of cells.

KAP-GFP efflux from the flagellum was calculated using Fick's law. The slope of the KAP-GFP background over the length of a flagellum was multiplied by the diffusion constant ($1.7 \mu\text{m}^2 \text{s}^{-1}$).

To calculate KAP-GFP influx, the KAP-GFP background was subtracted from the kymographs.

Then, the average intensity of anterograde trains was multiplied by the train frequency ($1.3 \text{ trains s}^{-1}$) to calculate the influx.

GFP photobleaching rate under TIR illumination was estimated by heavily decorating the coverslip surface with eGFP and calculating the rate of decrease in GFP fluorescence. To estimate the live-cell GFP photobleaching rate in *pf18 IFT27-GFP* cells, the fluorescent intensities of 94 anterograde trains from 9 cells were quantified at each time point en route to the flagellar tip. Each train's intensity profile was normalized by the mean intensity. The normalized intensity values were plotted against time and fit to a single exponential decay. The decay constant was used as the photobleaching rate.

Monte Carlo simulations

Monte Carlo simulations were performed to test the effect of limited number of GFPs per train and GFP photobleaching in PhotoGate experiments using the *pf18 IFT27-GFP* strain.

Experimentally measured values were used for the velocity and frequency of anterograde and retrograde trains. Simulations assumed that anterograde trains arrive and retrograde trains depart from the tip through a purely stochastic process adding particles to a mixed flagellar tip pool.

We estimated that each anterograde train contains 6 fluorescent GFPs by comparing the fluorescent intensities of anterograde trains in the *pf18 IFT27-GFP* strain to those of KAP-GFP

spots in the *fla3::KAP-GFP* strain under the same imaging conditions and calibrating the number of molecules based on previous photobleaching analysis of the *fla3::KAP-GFP* strain (Engel et al., 2009). Each retrograde train was constructed by a random selection of IFT particles available at the tip. Tip intensity measurements revealed that the signal of the IFT complexes located at the tip is approximately three times brighter than an average anterograde train. The photobleaching of GFPs (0.07 s^{-1}) under TIR illumination was accounted for in simulations and trains with at least one fluorescent GFP upon leaving the tip were marked detectable.

Simulations were also run to estimate the distribution of diffusing KAP molecules in the flagellum at a steady-state. In these simulations, previously reported values for the anterograde train injection rate ($1.3 \text{ trains s}^{-1}$) (Mueller et al., 2005) and the average number of KAP bound to a single anterograde train for each flagellar length (Engel et al., 2009) were used to estimate the number of KAP that arrives at the flagellar tip per second. KAP dissociated from the trains at the tip and immediately started one dimensional diffusion in the flagellum. The resting time of KAP at the tip was insignificant, and was not accounted for. The flagellum was modeled as a 5 - 12 μm long linear grid with spacing defined as the MSD of KAP diffusing at $1.7 \mu\text{m}^2 \text{ s}^{-1}$ (Figure 3h) during the time-step of the simulation (5 ms). At every time point, each active molecule had its grid position changed by +1 or -1. The molecules at the extreme terminus of the tip only moved towards the base. The diffusing KAP molecules were perfectly absorbed to the cell body as they arrived at the flagellar base (i.e. perfect sink) and exited the simulation. The simulations were run for 100,000 time points to allow molecules to reach a steady-state. The number of molecules at each grid position was calculated to plot the distribution of KAP molecules diffusing along the length of the flagellum. The total number of KAP was calculated by integrating the number of KAP diffusing along the entire flagellum and KAP on the anterograde trains. This number was

636 compared to a hypothetical scenario that KAP returns to the cell body with active transport. The
637 simulations were run 10 times to calculate the error.

638 Simulation codes are available on <https://github.com/SingleMoleculeAC/IFT-Dynamics>.

References

- Albee, A.J., Kwan, A.L., Lin, H., Granas, D., Stormo, G.D., and Dutcher, S.K. (2013). Identification of Cilia Genes That Affect Cell-Cycle Progression Using Whole-Genome Transcriptome Analysis in *Chlamydomonas reinhardtii*. *G3; Genes|Genomes|Genetics* 3, 979–991.
- Belyy, V., Shih, S.-M., Bandaria, J., Huang, Y., Lawrence, R.E., Zoncu, R., and Yildiz, A. (2017). PhotoGate microscopy to track single molecules in crowded environments. *Nat. Commun.* 8, 13978.
- Berthold, P., Schmitt, R., and Mages, W. (2002). An engineered *Streptomyces hygroscopicus* aph 7" gene mediates dominant resistance against hygromycin B in *Chlamydomonas reinhardtii*. *Protist* 153, 401–412.
- Blasius, T.L., Reed, N., Slepchenko, B.M., and Verhey, K.J. (2013). Recycling of Kinesin-1 Motors by Diffusion after Transport. *PLoS One* 8, 45–49.
- Broekhuis, J.R., Verhey, K.J., and Jansen, G. (2014). Regulation of cilium length and intraflagellar transport by the RCK-kinases ICK and MOK in renal epithelial cells. *PLoS One* 9.
- Brown, J.M., and Witman, G.B. (2014). Cilia and diseases. *Bioscience* 64, 1126–1137.
- Buisson, J., Chenouard, N., Lagache, T., Blisnick, T., Olivo-Marin, J.-C.J.-C., and Bastin, P. (2013). Intraflagellar transport proteins cycle between the flagellum and its base. *J. Cell Sci.* 126, 327–338.
- Chien A. (2017). IFT-Dynamics. GitHub. <https://github.com/SingleMoleculeAC/IFT-Dynamics>.
- Cole, D.G., Diener, D.R., Himmelblau, A.L., Beech, P.L., Fuster, J.C., and Rosenbaum, J.L. (1998). *Chlamydomonas* kinesin-II-dependent intraflagellar transport (IFT): IFT particles contain proteins required for ciliary assembly in *Caenorhabditis elegans* sensory neurons. *J. Cell Biol.* 141, 993–1008.
- Collingridge, P., Brownlee, C., and Wheeler, G.L. (2013). Compartmentalized calcium signaling in cilia regulates intraflagellar transport. *Curr. Biol.* 23, 2311–2318.
- Craft, J.M., Harris, J.A., Hyman, S., Kner, P., and Lehtreck, K.F. (2015). Tubulin transport by IFT is upregulated during ciliary growth by a cilium-autonomous mechanism. *J. Cell Biol.* 208, 223–237.
- Dentler, W. (2005). Intraflagellar transport (IFT) during assembly and disassembly of

Chlamydomonas flagella. *J. Cell Biol.* *170*, 649–659.

Engel, B.D., Ludington, W.B., and Marshall, W.F. (2009). Intraflagellar transport particle size scales inversely with flagellar length: Revisiting the balance-point length control model. *J. Cell Biol.* *187*, 81–89.

Engel, B.D., Ishikawa, H., Wemmer, K. a., Geimer, S., Wakabayashi, K.I., Hirono, M., Craige, B., Pazour, G.J., Witman, G.B., Kamiya, R., et al. (2012). The role of retrograde intraflagellar transport in flagellar assembly, maintenance, and function. *J. Cell Biol.* *199*, 151–167.

Firestone, A.J., Weinger, J.S., Maldonado, M., Barlan, K., Langston, L.D., O'Donnell, M., Gelfand, V.I., Kapoor, T.M., Chen, J.K., O'Donnell, M., et al. (2012). Small-molecule inhibitors of the AAA+ ATPase motor cytoplasmic dynein. *Nature* *484*, 125–129.

Harris, J.A., Liu, Y., Yang, P., Kner, P., and Lehtrekk, K.F. (2016). Single-particle imaging reveals intraflagellar transport-independent transport and accumulation of EB1 in *Chlamydomonas* flagella. *Mol. Biol. Cell* *27*, 295–307.

Helenius, J., Brouhard, G., Kalaidzidis, Y., Diez, S., and Howard, J. (2006). The depolymerizing kinesin MCAK uses lattice diffusion to rapidly target microtubule ends. *Nature* *441*, 115–119.

Hendel, N.L., Thomson, M., and Marshall, W.F. (2017). Diffusion as a ruler: Modeling kinesin diffusion as a length sensor for intraflagellar transport. *bioRxiv Prepr.*

Iomini, C., Babaev-Khaimov, V., Sassaroli, M., and Piperno, G. (2001). Protein particles in *Chlamydomonas* flagella undergo a transport cycle consisting of four phases. *J. Cell Biol.* *153*, 13–24.

Ishikawa, H., and Marshall, W.F. (2011). Ciliogenesis: building the cell's antenna. *Nat Rev Mol Cell Biol* *12*, 222–234.

Kozminski, K.G., Johnson, K. a, Forscher, P., and Rosenbaum, J.L. (1993). A motility in the eukaryotic flagellum unrelated to flagellar beating. *Proc. Natl. Acad. Sci. U. S. A.* *90*, 5519–5523.

Kozminski, K.G., Beech, P.L., and Rosenbaum, J.L. (1995). The *Chlamydomonas* kinesin-like protein FLA10 is involved in motility associated with the flagellar membrane. *J. Cell Biol.* *131*, 1517–1527.

Laib, J.A., Marin, J.A., Bloodgood, R.A., and Guilford, W.H. (2009). The reciprocal coordination and mechanics of molecular motors in living cells. *Proc Natl Acad Sci U S A* *106*, 3190–3195.

701 Lechtreck, K.-F., Johnson, E.C., Sakai, T., Cochran, D., Ballif, B. a, Rush, J., Pazour, G.J., Ikebe,
 702 M., and Witman, G.B. (2009). The Chlamydomonas reinhardtii BBSome is an IFT cargo
 703 required for export of specific signaling proteins from flagella. *J. Cell Biol.* 187, 1117–1132.
 704 Lechtreck, K.F., Van De Weghe, J.C., Harris, J.A., and Liu, P. (2017). Protein transport in
 705 growing and steady-state cilia. *Traffic*.
 706 Lefebvre, P. a, and Rosenbaum, J.L. (1986). Regulation of the synthesis and assembly of ciliary
 707 and flagellar proteins during regeneration. *Annu. Rev. Cell Biol.* 2, 517–546.
 708 Levy, E.M. (1974). Flagellar elongation as a moving boundary problem. *Bull. Math. Biol.* 36,
 709 265–273.
 710 Li, W., Yi, P., and Ou, G. (2015). Somatic CRISPR-Cas9-induced mutations reveal roles of
 711 embryonically essential dynein chains in Caenorhabditis elegans cilia. *J. Cell Biol.* 208, 683–
 712 692.
 713 Liang, Y., Pang, Y., Wu, Q., Hu, Z., Han, X., Xu, Y., Deng, H., and Pan, J. (2014). FLA8/KIF3B
 714 Phosphorylation Regulates Kinesin-II Interaction with IFT-B to Control IFT Entry and
 715 Turnaround. *Dev. Cell* 30, 585–597.
 716 Ludington, W.B., Wemmer, K. a, Lechtreck, K.F., Witman, G.B., and Marshall, W.F. (2013).
 717 Avalanche-like behavior in ciliary import. *Proc. Natl. Acad. Sci. U. S. A.* 110, 3925–3930.
 718 Ludington, W.B., Ishikawa, H., Serebrenik, Y. V., Ritter, A., Hernandez-Lopez, R.A.,
 719 Gunzenhauser, J., Kannegaard, E., and Marshall, W.F. (2015). A systematic comparison of
 720 mathematical models for inherent measurement of ciliary length: How a cell can measure length
 721 and volume. *Biophys. J.* 108, 1361–1379.
 722 Marshall, W.F., and Rosenbaum, J.L. (2001). Intraflagellar transport balances continuous
 723 turnover of outer doublet microtubules: implications for flagellar length control. *J. Cell Biol.*
 724 155, 405–414.
 725 Marshall, W., Qin, H., Brenni, M., and Rosenbaum, J. (2005). Flagellar Length Control System:
 726 Testing a Simple Model Based on Intraflagellar Transport and Turnover. *Mol. Biol. Cell* 16, 270–
 727 278.
 728 Mijalkovic, J., Prevo, B., Oswald, F., Mangeol, P., and Peterman, E.J.G. (2017). Ensemble and
 729 single-molecule dynamics of IFT dynein in Caenorhabditis elegans cilia. *Nat. Commun.* 8,
 730 14591.
 731 Mueller, J., Perrone, C.A., Bower, R., Cole, D.G., and Porter, M.E. (2005). The FLA3 KAP

732 Subunit Is Required for Localization of Kinesin-2 to the Site of Flagellar Assembly and
 733 Processive Anterograde Intraflagellar Transport. *Mol. Biol. Cell* *16*, 1341–1354.
 734 Nakamura, S., Takino, H., and Kojima, M.K. (1987). Effect of Lithium on Flagellar Length in
 735 *Chlamydomonas reinhardtii*. *Cell Struct. Funct.* *12*, 369–374.
 736 Nguyen, R.L., Tam, L.W., and Lefebvre, P.A. (2005). The LF1 gene of *Chlamydomonas*
 737 *reinhardtii* encodes a novel protein required for flagellar length control. *Genetics* *169*, 1415–
 738 1424.
 739 Pan, J., and Snell, W.J. (2005). *Chlamydomonas* shortens its flagella by activating axonemal
 740 disassembly, stimulating IFT particle trafficking, and blocking anterograde cargo loading. *Dev.*
 741 *Cell* *9*, 431–438.
 742 Pazour, G.J., Dickert, B.L., and Witman, G.B. (1999). The DHC1b (DHC2) isoform of
 743 cytoplasmic dynein is required for flagellar assembly. *J Cell Biol* *144*, 473–481.
 744 Pedersen, L.B., Geimer, S., and Rosenbaum, J.L. (2006). Dissecting the molecular mechanisms
 745 of intraflagellar transport in *Chlamydomonas*. *Curr. Biol.* *16*, 450–459.
 746 Perrone, C.A., Triticchler, D., Patrick, T., Raqual, B., Yoder, B.K., and Porter, M.E. (2003). A
 747 Novel Dynein Light Intermediate Chain Colocalizes with the Retrograde Motor for Intraflagellar
 748 Transport at Sites of Axoneme Assembly in *Chlamydomonas* and Mammalian Cells. *Mol. Biol.*
 749 *Cell* *14*, 2559–2569.
 750 Pigino, G., Geimer, S., Lanzavecchia, S., Paccagnini, E., Cantele, F., Diener, D.R., Rosenbaum,
 751 J.L., and Lupetti, P. (2009). Electron-tomographic analysis of intraflagellar transport particle
 752 trains in situ. *J. Cell Biol.* *187*, 135–148.
 753 Porter, M.E., Bower, R., Knott, J.A., Byrd, P., and Dentler, W. (1999). Cytoplasmic dynein heavy
 754 chain 1b is required for flagellar assembly in *Chlamydomonas*. *Mol. Biol. Cell* *10*, 693–712.
 755 Prevo, B., Mangeol, P., Oswald, F., Scholey, J.M., and Peterman, E.J.G. (2015). Functional
 756 differentiation of cooperating kinesin-2 motors orchestrates cargo import and transport in *C.*
 757 *elegans* cilia. *Nat. Cell Biol.* *17*, 1536–1545.
 758 Prevo, B., Scholey, J.M., and Peterman, E.J.G. (2017). Intraflagellar transport: Mechanisms of
 759 motor action, cooperation, and cargo delivery. *FEBS J.*
 760 Qin, H., Diener, D.R., Geimer, S., Cole, D.G., and Rosenbaum, J.L. (2004). Intraflagellar
 761 transport (IFT) cargo: IFT transports flagellar precursors to the tip and turnover products to the
 762 cell body. *J. Cell Biol.* *164*, 255–266.

763 Qin, H., Wang, Z., Diener, D., Rosenbaum, J., Hongmin Qin, Zhaohui Wang, Dennis Diener, and
 764 J.R., Qin, H., Wang, Z., Diener, D., and Rosenbaum, J. (2007). Intraflagellar Transport Protein 27
 765 Is a Small G Protein Involved in Cell-Cycle Control. *Curr. Biol.* 17, 193–202.
 766 Rasala, B.A., Barrera, D.J., Ng, J., Plucinak, T.M., Rosenberg, J.N., Weeks, D.P., Oyler, G.A.,
 767 Peterson, T.C., Haerizadeh, F., and Mayfield, S.P. (2013). Expanding the spectral palette of
 768 fluorescent proteins for the green microalga *Chlamydomonas reinhardtii*. *Plant J.* 74, 545–556.
 769 Reck, J., Schauer, A.M., VanderWaal Mills, K., Bower, R., Tritschler, D., Perrone, C.A., and
 770 Porter, M.E. (2016). The role of the dynein light intermediate chain in retrograde IFT and
 771 flagellar function in *Chlamydomonas*. *Mol. Biol. Cell* 27, 2404–2422.
 772 Renault, T.T., Abraham, A.O., Bergmiller, T., Paradis, G., Rainville, S., Charpentier, E., Guet,
 773 C.C., Tu, Y., Namba, K., Keener, J.P., et al. (2017). Bacterial flagella grow through an injection-
 774 diffusion mechanism. *Elife* 6, e23136.
 775 Ringo, D.L. (1967). Flagellar motion and fine structure of the flagellar apparatus in
 776 *Chlamydomonas*. *J. Cell Biol.* 543–571.
 777 Rompolas, P., Pedersen, L.B., Patel-King, R.S., and King, S.M. (2007). *Chlamydomonas*
 778 FAP133 is a dynein intermediate chain associated with the retrograde intraflagellar transport
 779 motor. *J Cell Sci* 120, 3653–3665.
 780 Rosenbaum, J.L., Moulder, J.E., and Ringo, D.L. (1969). Flagellar elongation and shortening in
 781 *Chlamydomonas*. The use of cycloheximide and colchicine to study the synthesis and assembly
 782 of flagellar proteins. *J. Cell Biol.* 41, 600–619.
 783 Satir, P., Pedersen, L.B., and Christensen, S.T. (2010). The primary cilium at a glance. *J. Cell Sci.*
 784 123, 499–503.
 785 Satish Tammana, T. V, Tammana, D., Diener, D.R., Rosenbaum, J., Tammana, T.V.S., Tammana,
 786 D., Diener, D.R., and Rosenbaum, J. (2013). Centrosomal protein CEP104 (*Chlamydomonas*
 787 FAP256) moves to the ciliary tip during ciliary assembly. *J. Cell Sci.* 126, 5018–5029.
 788 Shih, S.M., Engel, B.D., Kocabas, F., Bilyard, T., Gennerich, A., Marshall, W.F., and Yildiz, A.
 789 (2013). Intraflagellar transport drives flagellar surface motility. *Elife* 2, e00744.
 790 Signor, D., Wedatman, K.P., Orozco, J.T., Dwyer, N.D., Bargmann, C.I., Rose, L.S., and Scholey,
 791 J.M. (1999). Role of a class DHC1b dynein in retrograde transport of IFT motors and IFT raft
 792 particles along cilia, but not dendrites, in chemosensory neurons of living *Caenorhabditis*
 793 *elegans*. *J. Cell Biol.* 147, 519–530.

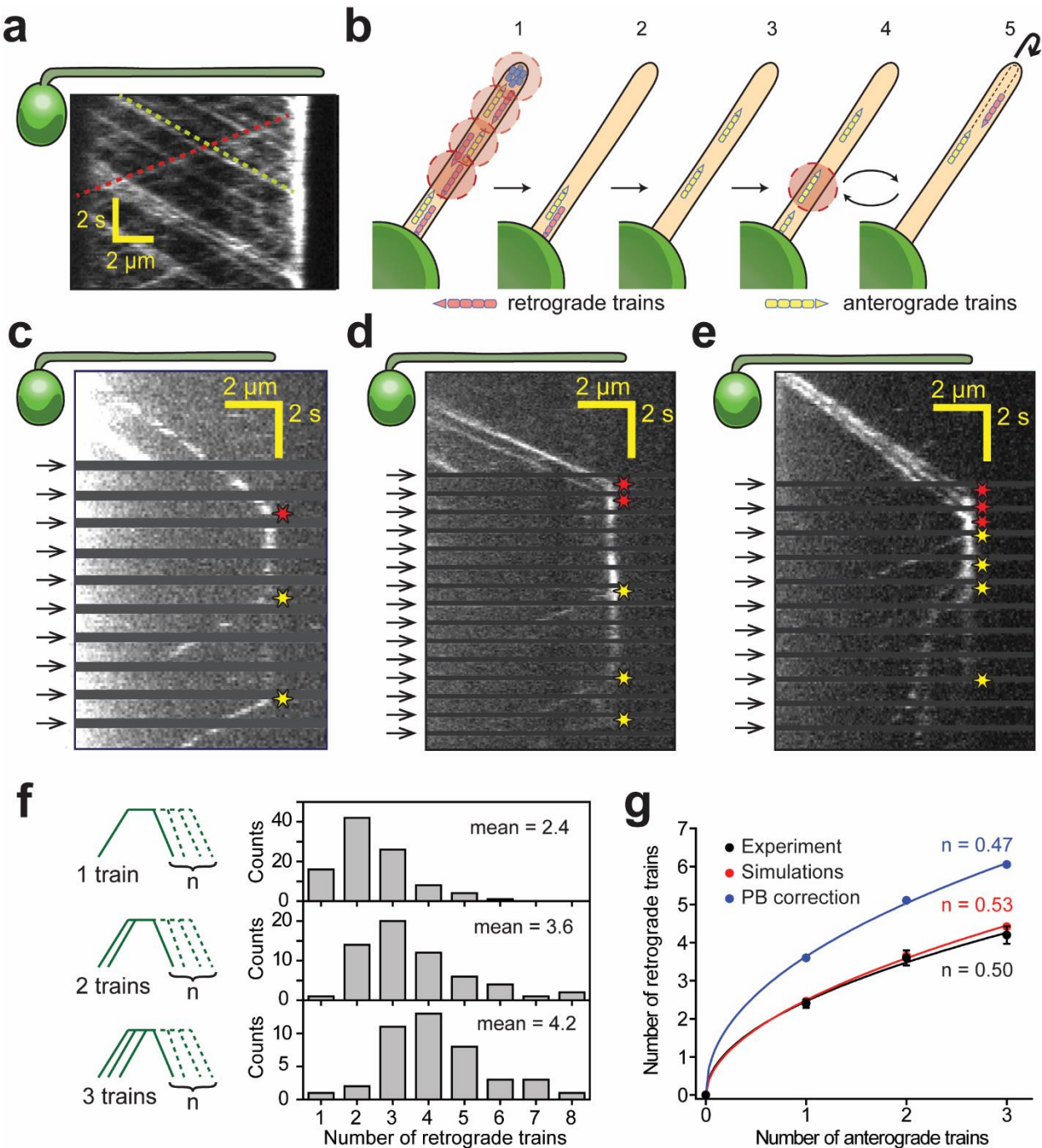
794 Snow, J.J., Ou, G., Gunnarson, A.L., Walker, M.R.S., Zhou, H.M., Brust-Mascher, I., and
 795 Scholey, J.M. (2004). Two anterograde intraflagellar transport motors cooperate to build sensory
 796 cilia on *C. elegans* neurons. *Nat. Cell Biol.* 6, 1109–1113.
 797 Stepanek, L., and Pigino, G. (2016). Microtubule doublets are double-track railways for
 798 intraflagellar transport trains. *Science* 352, 721–724.
 799 Stolc, V., Samanta, M.P., Tongprasit, W., and Marshall, W.F. (2005). Genome-wide
 800 transcriptional analysis of flagellar regeneration in *Chlamydomonas reinhardtii* identifies
 801 orthologs of ciliary disease genes. *Proc Natl Acad Sci U S A* 102, 3703–3707.
 802 Tam, L.W., Wilson, N.F., and Lefebvre, P.A. (2007). A CDK-related kinase regulates the length
 803 and assembly of flagella in *Chlamydomonas*. *J. Cell Biol.* 176, 819–829.
 804 Toropova, K., Mladenov, M., and Roberts, A.J. (2017). Intraflagellar transport dynein is
 805 autoinhibited by trapping of its mechanical and track-binding elements Toropova, K., Mladenov,
 806 M., & Roberts, A. J. (2017). Intraflagellar transport dynein is autoinhibited by trapping of its
 807 mechanical and track-binding . *Nat. Struct. Mol. Biol.* 56, 1–6.
 808 Wang, Z., Fan, Z.C., Williamson, S.M., and Qin, H. (2009). Intraflagellar transport (IFT) protein
 809 IFT25 is a phosphoprotein component of IFT complex B and physically interacts with IFT27 in
 810 *Chlamydomonas*. *PLoS One* 4.
 811 Williams, C.L., McIntyre, J.C., Norris, S.R., Jenkins, P.M., Zhang, L., Pei, Q., Verhey, K., and
 812 Martens, J.R. (2014). Direct evidence for BBSome-associated intraflagellar transport reveals
 813 distinct properties of native mammalian cilia. *Nat. Commun.* 5, 5813.
 814 Wilson, N.F., and Lefebvre, P. a (2004). Regulation of Flagellar Assembly by Glycogen Synthase
 815 Kinase 3 in *Chlamydomonas reinhardtii* Regulation of Flagellar Assembly by Glycogen Synthase
 816 Kinase 3 in *Chlamydomonas reinhardtii*. *Eukaryot. Cell* 3, 1307–1319.
 817 Wingfield, J.L., Mengoni, I., Bomberger, H., Jiang, Y.Y., Walsh, J.D., Brown, J.M., Picariello, T.,
 818 Cochran, D.A., Zhu, B., Pan, J., et al. (2017). IFT trains in different stages of assembly queue at
 819 the ciliary base for consecutive release into the cilium. *Elife* 6, 1–27.
 820 Wren, K.N., Craft, J.M., Tritschler, D., Schauer, A., Patel, D.K., Smith, E.F., Porter, M.E., Kner,
 821 P., and Lehtreck, K.F. (2013). A differential cargo-loading model of ciliary length regulation by
 822 IFT. *Curr. Biol.* 23, 2463–2471.
 823 Yi, P., Li, W.J., Dong, M.Q., and Ou, G. (2017). Dynein-Driven Retrograde Intraflagellar
 824 Transport Is Triphasic in *C. elegans* Sensory Cilia. *Curr. Biol.* 27, 1448–1461.e7.

825 Zhang, K., Foster, H.E., Rondelet, A., Lacey, S.E., Bahi-Buisson, N., Bird, A.W., and Carter, A.P.
826 (2017). Cryo-EM Reveals How Human Cytoplasmic Dynein Is Auto-inhibited and Activated.
827 Cell 169, 1303–1314.e18.

828

829 **Acknowledgments**

830 We would like to thank K. Augsperger for assistance with the isolation and screening of the
831 *D1bLIC-Cherry KAP-GFP* tagged strains, V. Belyy, J. Bandaria, and P. Qin for technical
832 assistance, and W. F. Marshall and N. L. Hendel for sharing results prior to publication. This
833 work has been supported by NIH (GM094522, GM116204 (AY), GM055667 (MEP)), and NSF
834 (MCB-1055017 and MCB-1617028 (AY)).



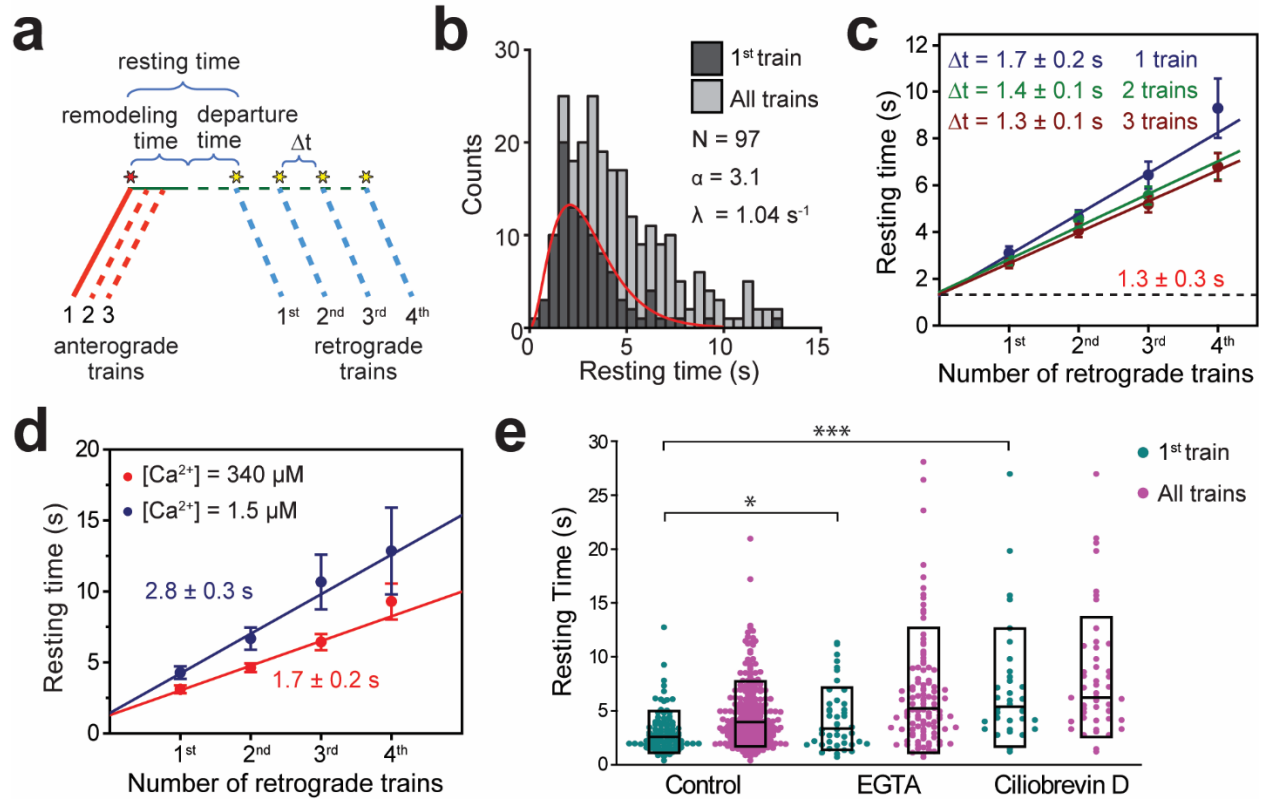
836

837 **Figure 1. IFT trains split apart and mix with each other at the flagellar tip.**

838 (a) Kymograph of a surface-immobilized *pf18* IFT27-GFP strain shows that IFT trains move

839 bidirectionally along the flagellum, only reversing direction at the tip and the base. Multiple IFT

840 trains accumulate at the flagellar tip. Representative anterograde and retrograde trajectories are
 841 shown with yellow and red dashed lines, respectively. **(b)** Schematic representation of the
 842 PhotoGate assay. 1) The distal half of the flagellum is prebleached by moving the powerful gate
 843 beam from the flagellar tip to near the base of the flagellum. 2-3) The gate beam is turned off to
 844 allow a single anterograde train to enter the flagellum without photobleaching. 4) The beam is
 845 then repeatedly turned on to photobleach the successive trains entering the flagellum and 5)
 846 turned off for 0.8 s to image the single fluorescent train within the flagellum. Photobleached
 847 trains are not shown. **(c-e)** Kymographs of one (c), two (d) and three (e) fluorescent anterograde
 848 trains entering the flagellum. Anterograde trains pause at the flagellar tip and split into multiple
 849 retrograde trains that move back to the base. Arrival of fluorescent anterograde trains and
 850 departure of retrograde trains at the tip are shown with red and yellow stars, respectively. Arrows
 851 represent repetitive bleaching events near the base of the flagellum. **(f)** (Left) The number of
 852 fluorescent retrograde trains was quantified as a function of one, two or three fluorescent
 853 anterograde trains entering the flagellum after photobleaching. (Right) The average number of
 854 retrograde trains increased sub-proportionally with the number of fluorescent anterograde trains
 855 entering the flagellum. $N = 97, 60, 42$ train events from top to bottom, in 160 cells, from 13
 856 independent experiments. **(g)** The number of detectable retrograde trains versus the numbers of
 857 incoming anterograde trains in PhotoGate experiments and Monte Carlo simulations (PB:
 858 photobleaching). Solid lines represent the fit of data to the power law ($y = ax^n$). n is less than 1
 859 under each condition. Error bars represent s.e.m. ($N = 10,000$ for simulations).



861

862 **Figure 2. Tip turnaround of IFT trains is a multistep process regulated by dynein activity**
 863 **and extracellular Ca^{2+} .**

864 (a) The schematic describes the definition of tip resting time, remodeling time, and departure
 865 time measured from the kymographs. Arrival of the first fluorescent anterograde train and the
 866 departure of retrograde trains are shown with red and yellow stars, respectively. Tip resting time
 867 and departure time are only shown for the first retrograde train. Tip remodeling time is assumed
 868 to be the same for each train. Δt represents the time between the departure of successive
 869 retrograde trains. (b) The resting time histogram of the first retrograde IFT27-GFP train (dark
 870 grey) and all of the trains (light grey) emanating from a single anterograde train. The histogram
 871 of the first retrograde trains was fitted to a Gamma function (red curve). α and λ are shape and
 872 rate parameters, respectively. (c) The linear fit to the average tip resting time reveals Δt between
 873 successive trains. The y-intercept (black dashed line) represents the tip remodeling time. Errors

874 represent standard error of the linear fit. **(d)** Average tip resting times of the 1st, 2nd, 3rd and 4th
875 retrograde IFT27-GFP trains coming out of an anterograde train for cells in TAP media (red, N =
876 97) and calcium-depleted media (blue, N = 44). Errors represent standard error of the linear fit.
877 **(e)** IFT27-GFP tip resting times in 0.5 mM EGTA and 0.1 mM ciliobrevin D treated cells. The
878 line within the boxplot represents the mean. The outer edges of the box represent standard
879 deviation. N = 97, 44, 34, 34, 52 retrograde trains from left to right, in a total of 22 independent
880 experiments (Welch's t-test, *p < 0.05, ***p < 0.001, as compared to no treatment for first
881 retrograde trains).

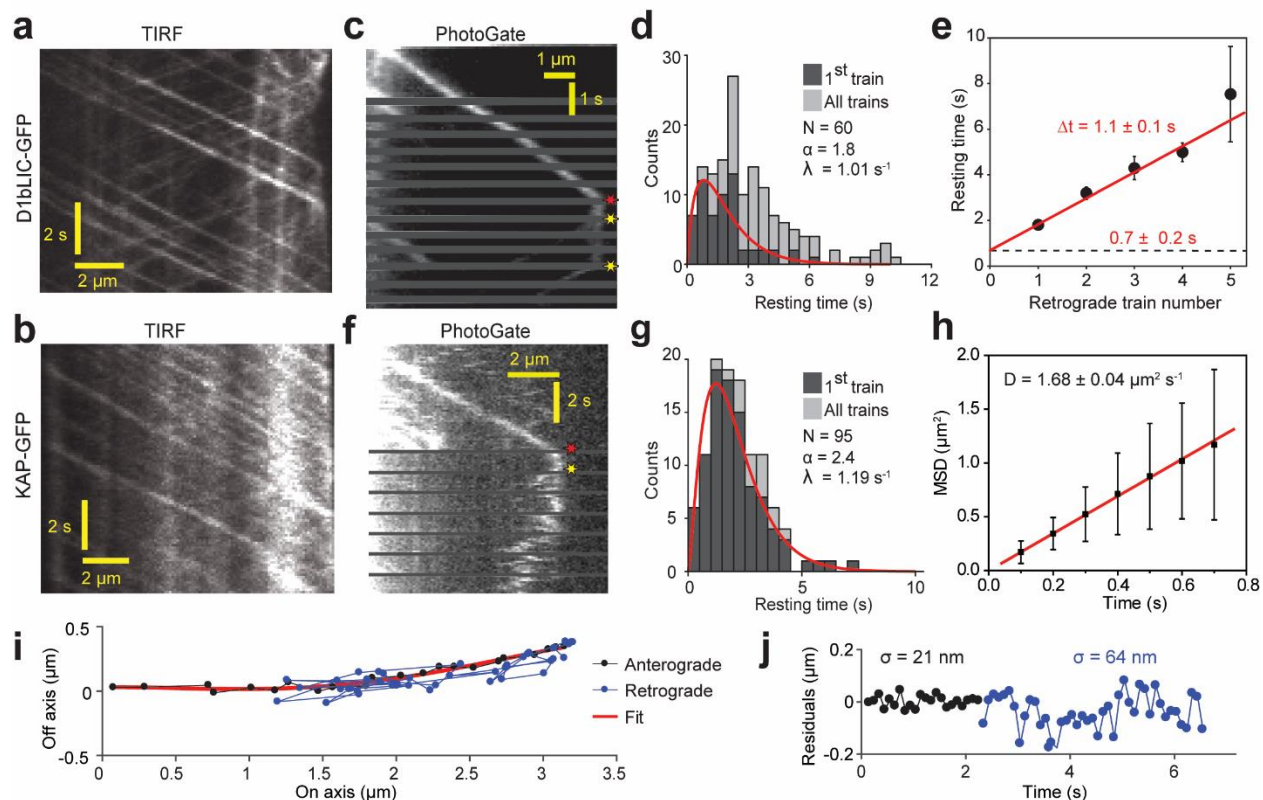


Figure 3. PhotoGate reveals the tip turnaround behavior of IFT motors.

(a) In a conventional TIR assay, anterograde and retrograde D1bLIC-GFP traces were clearly visible, but the tip behavior of individual trains could not be discerned. (b) In a conventional TIR assay, KAP-GFP was observed to move anterogradely, but the retrograde transport of KAP was rarely observed. (c) PhotoGate imaging of D1bLIC-GFP shows that D1bLIC trains move to the tip anterogradely, split into multiple trains, and return to the base retrogradely. Red and yellow stars indicate arrival to and departure of D1bLIC-GFP from the tip, respectively. (d) The tip resting time histogram of D1bLIC-GFP. Tip resting time of the first retrograde trains are fit to a Gamma distribution (red curve; 95% c.i. for α is 1.30-2.52 and for λ is 0.69-1.47 s^{-1}). $N = 60$ anterograde trains in 60 cells over 9 independent experiments. (e) Averaged tip resting time of the 1st, 2nd, 3rd, and 4th retrograde D1bLIC-GFP particles returning from the tip (mean \pm s.e.m.). (f) Kymograph analysis of a KAP-GFP cell imaged by PhotoGate. KAP undergoes active

895 transport in the anterograde direction, pauses at the flagellar tip, and diffuses back to the flagellar
896 base. **(g)** The tip resting time histogram of KAP-GFP. The red curve represents a fit of first train
897 resting times to a Gamma distribution. $N = 95$ anterograde trains in 47 cells over 4 independent
898 experiments (95% c.i. for α is 1.87-3.19 and for λ is 0.88-1.60 s^{-1}). **(h)** MSD analysis of KAP-
899 GFP movement after it leaves the flagellar tip. The average diffusion constant is $1.68 \pm 0.04 \mu\text{m}^2$
900 s^{-1} ($N = 27$, mean \pm s.e.m.). **(i)** High-resolution tracking of a KAP-GFP particle reveals the two-
901 dimensional trajectory during anterograde (black) and diffusion (blue). The red curve is the
902 polynomial fit to the trace. **(j)** The residual plot to the trace in (i) reveals lateral fluctuations
903 during anterograde transport (black) and diffusive (blue) movement.

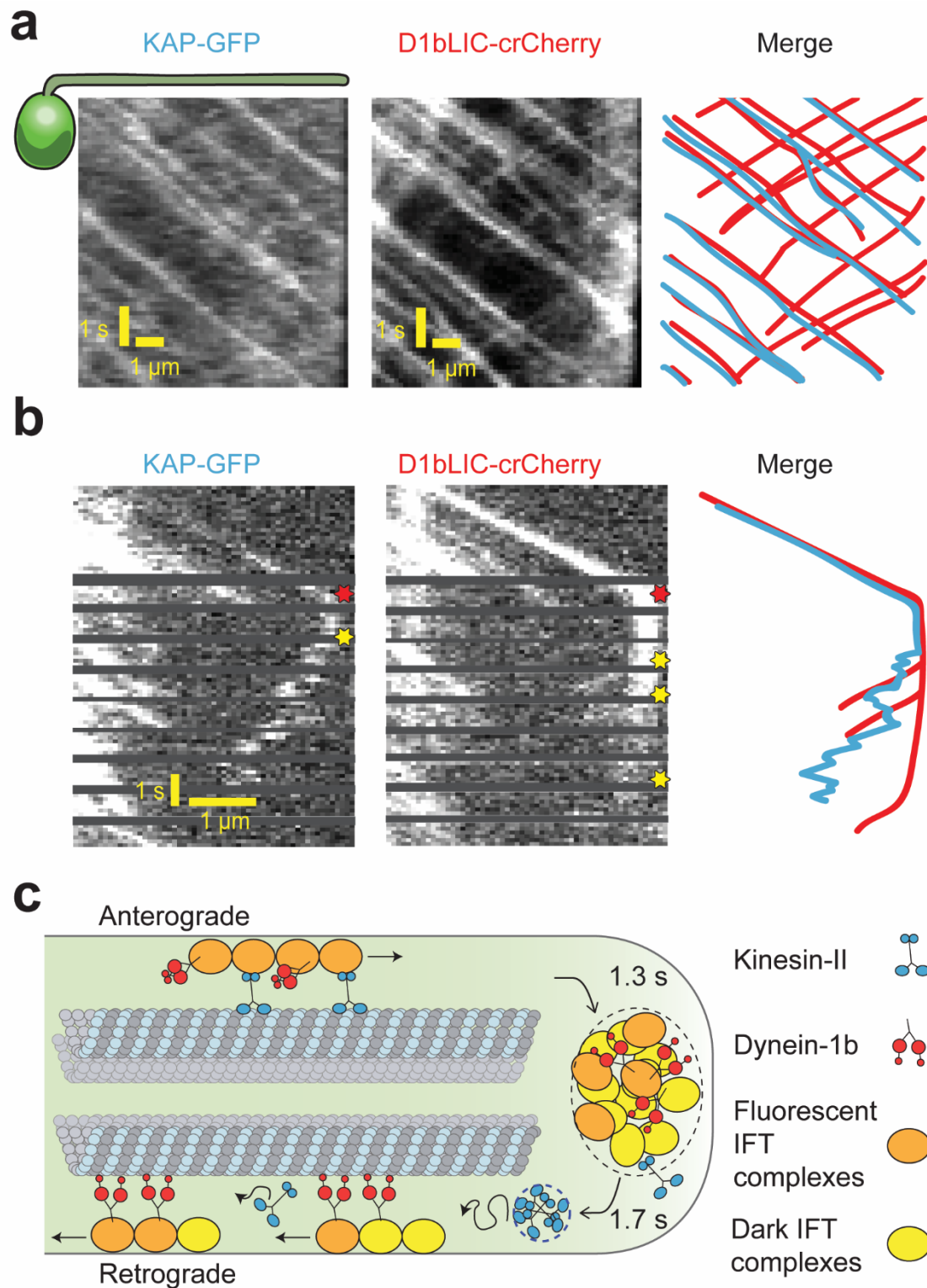


Figure 4. Transport roles of kinesin-II and dynein-1b.

(a) Representative kymographs of KAP-GFP and D1bLIC-crCherry in a *dlb1c::D1bLIC-*

907 *crCherry KAP-GFP* flagellum. KAP-GFP and D1bLIC-crCherry co-localize on the IFT trains in
908 the anterograde direction. Retrograde tracks are seen in the D1bLIC-crCherry channel, but are
909 rarely visible in the KAP-GFP channel. **(b)** Example two-color PhotoGate trace of KAP-GFP
910 (left) and D1bLIC-crCherry (middle) in single flagella. KAP-GFP and D1bLIC-crCherry arrive
911 at the tip on the same train. In this example, KAP diffuses away from the tip before the departure
912 of D1bLIC trains (right). Red and yellow stars indicate arrival to and departure from the flagellar
913 tip, respectively. **(c)** A model for the turnover of IFT trains and motors at the flagellar tip.
914 Kinesin-II motors transport individual anterograde IFT trains to the flagellar tip. Dynein-1b is
915 carried with anterograde trains as an inactive passenger. At the tip, IFT complexes detach from
916 microtubules, disassemble, and mix with the tip protein pool to assemble new trains. These trains
917 are transported retrogradely by dynein-1b. Kinesin-II detaches from IFT trains at the flagellar tip
918 and diffuses back to the base by diffusion either as a cluster (blue dashed circle) or individually.
919

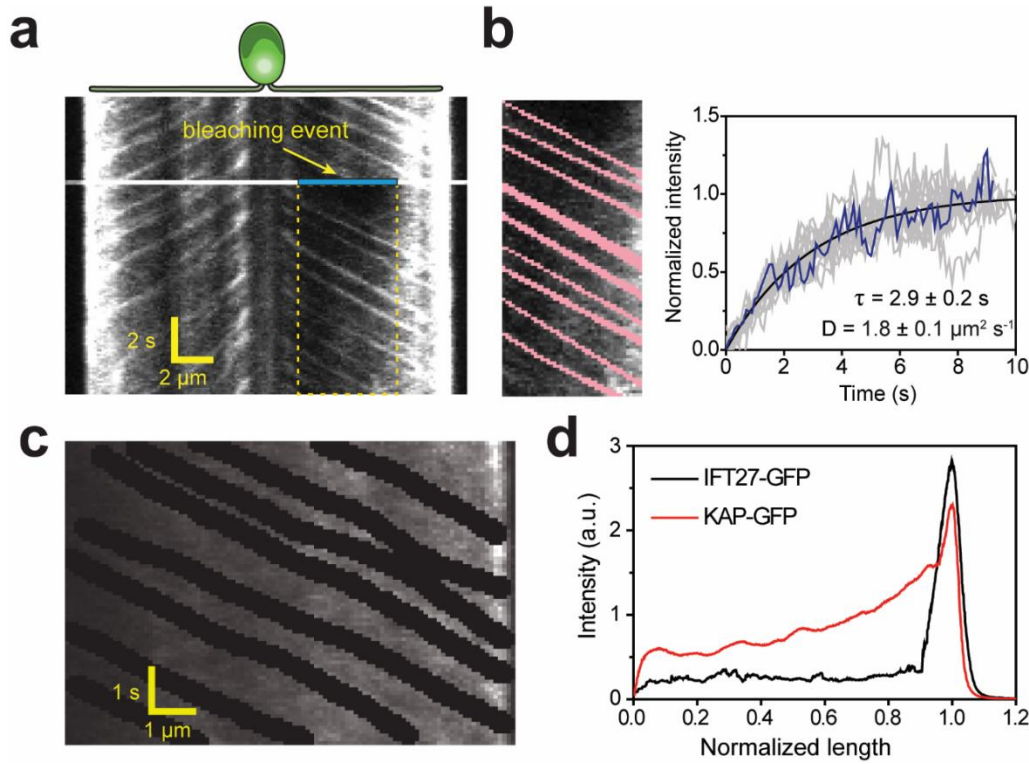


Figure 5. Diffusion of KAP from the flagellar tip leads to a concentration gradient along the flagellum.

(a) Kymograph of KAP-GFP movement before and after photobleaching the middle section of the flagellum (blue area). While fluorescence recovery from the base is through anterograde movement, the recovery from the tip region is due to diffusion. (b) (Left) The GFP signal of anterograde traces (red) was manually subtracted from the rectangular area shown in (a). (Right) The intensity in the photobleached area shows recovery as a function of time (blue line). The average recovery signal of 13 cells (grey lines) was fitted to a one-dimensional diffusion equation (black curve, $\pm 95\%$ c.i.). (c) In conventional TIR imaging, anterograde trajectories of KAP-GFP were manually subtracted from the kymograph. (d) The average GFP signal along the length of a flagellum in KAP-GFP and IFT27-GFP cells after the removal of anterograde and retrograde transport traces from the kymographs. Flagellar base and tip positions were normalized to 0 and 1, respectively. $N = 11$ for both KAP-GFP and IFT27-GFP.

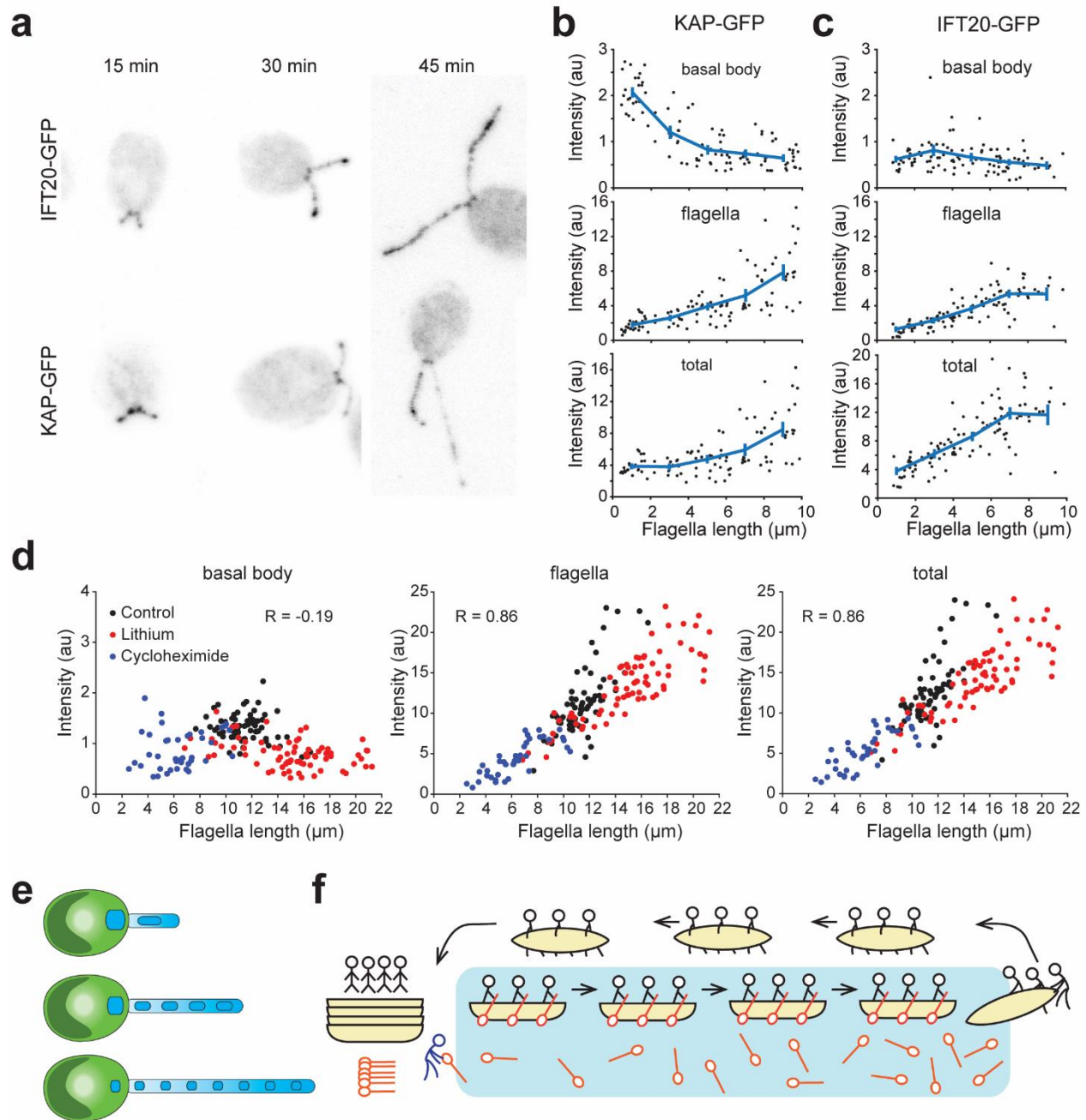
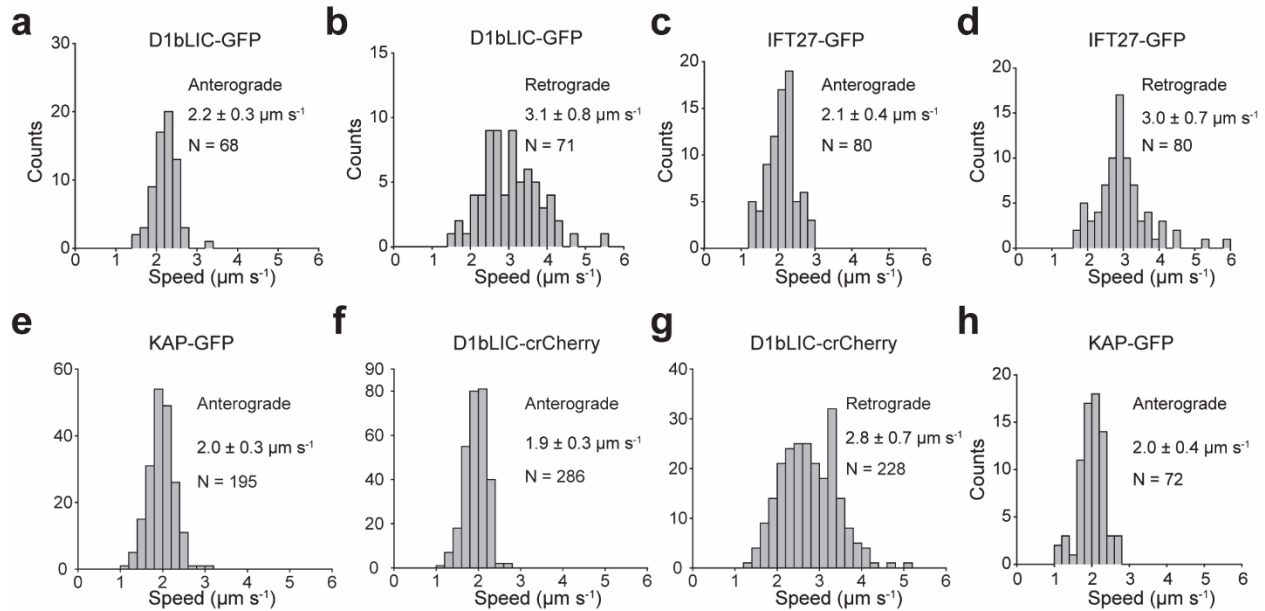


Figure 6. Kinesin-II accumulates in flagella and is depleted at the basal body during flagellar growth.

(a) Representative confocal images show the distribution of IFT20-GFP and KAP-GFP fluorescence at the basal body region and in the flagella during flagellar regrowth. (b,c) Integrated KAP-GFP (b) and IFT20-GFP (c) fluorescence at the basal body (top), in the

940 flagellum (middle), and in both regions (bottom) at different flagellar lengths. Each black dot
941 represents a single flagellum and the blue line is the running average (\pm s.e.m.). For KAP-GFP, N
942 = 104 flagella from 70 cells over 2 independent experiments. For IFT20-GFP, N = 103 flagella
943 from 56 cells over 2 independent experiments. **(d)** Integrated KAP-GFP fluorescence at the basal
944 body (left), in the flagellum (middle), and in both regions (right) in control cells was compared to
945 cells treated with 50 mM Li^+ , and cells that regrow their flagella after cycloheximide treatment.
946 R represents Pearson's correlation coefficient. Each dot represents a single flagellum. For control
947 cells, N = 66 flagella from 33 cells. For lithium-treated cells, N = 74 flagella from 37 cells. For
948 cycloheximide-treated cells, N = 40 flagella from 20 cells. **(e)** A model for flagellar length
949 control. When the flagellum is short, IFT trains contain more kinesin-II from the large basal body
950 pool. As flagella elongate, the number of kinesin-II per IFT train decreases because a significant
951 fraction of the kinesin-II unloads at the tip and undergoes diffusion in the flagellar lumen,
952 depleting the kinesin-II pool at the flagellar base. **(f)** An analogy for kinesin-II loading on IFT
953 trains. Passengers (dynein-1b) travel from the left shore (basal body) to the right shore (flagellar
954 tip) on a boat (IFT trains) with oars (kinesin-II). At the right shore, the passengers get out and
955 walk the boats back to the dock. Oars are left on the water and can only be collected when they
956 randomly float back to the left shore. If the distance between the shores is large, oars build up on
957 the water and are not readily available for new boats at the left shore.

959 **1. Figure Supplements**



960 **Figure 1-Figure Supplement 1. Anterograde and retrograde velocities of epitope-tagged**
 961 **IFT27, KAP, and D1bLIC.**

962 **(a,b)** Anterograde (a) and retrograde (b) velocities of D1bLIC-GFP in *dlb1c::D1bLIC-GFP*
 963 cells. **(c, d)** Anterograde (c) and retrograde (d) velocities of IFT27-GFP in *pfl18 IFT-27-GFP*
 964 cells. **(e)** Anterograde velocities of KAP-GFP in *dlb1c::D1bLIC-crCherry KAP-GFP* cells. **(f, g)**
 965 Anterograde (f) and retrograde (g) velocities of D1bLIC-crCherry in *dlb1c::D1bLIC-crCherry*
 966 *KAP-GFP* cells. **(h)** Anterograde velocities of KAP-GFP in *fla3::KAP-GFP* cells. All velocities
 967 are reported as mean \pm s.d. N represents the number of trains measured.

968

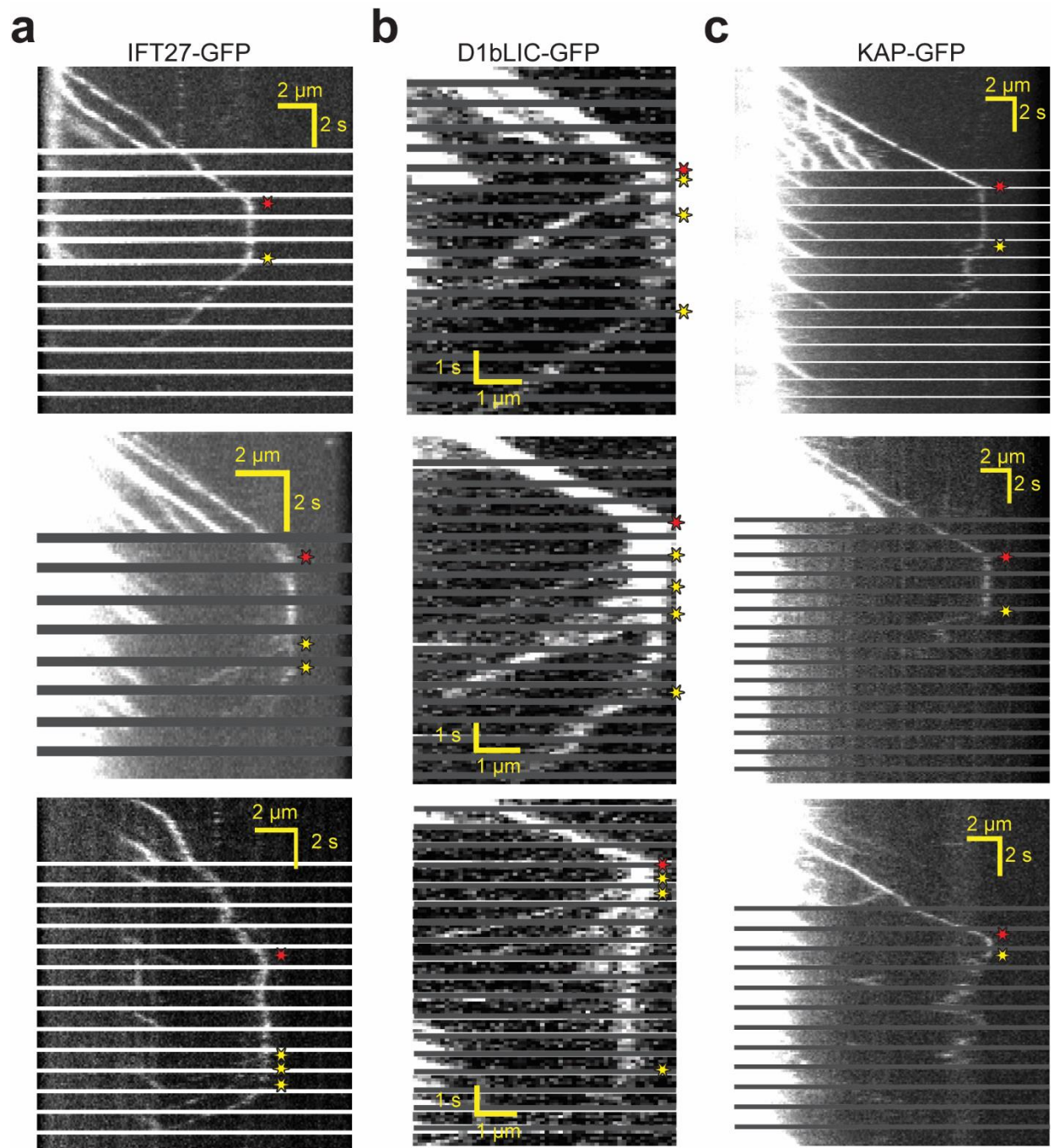


Figure 1-Figure Supplement 2. Additional examples for PhotoGate imaging of IFT27, D1bLIC, and KAP.

(a) IFT27 is moved to the tip on anterograde trains, remodels, and returns to the flagellar base on retrograde trains. **(b)** Dynein is moved to the tip on anterograde trains, remodels, and moves

974 retrogradely to the cell body. (c) Kinesin moves anterograde trains to the flagellar tip, dissociates
975 from the IFT trains at the tip, and diffuses within the flagellum. Red and yellow stars indicate
976 arrival to and departure from the tip, respectively.

977

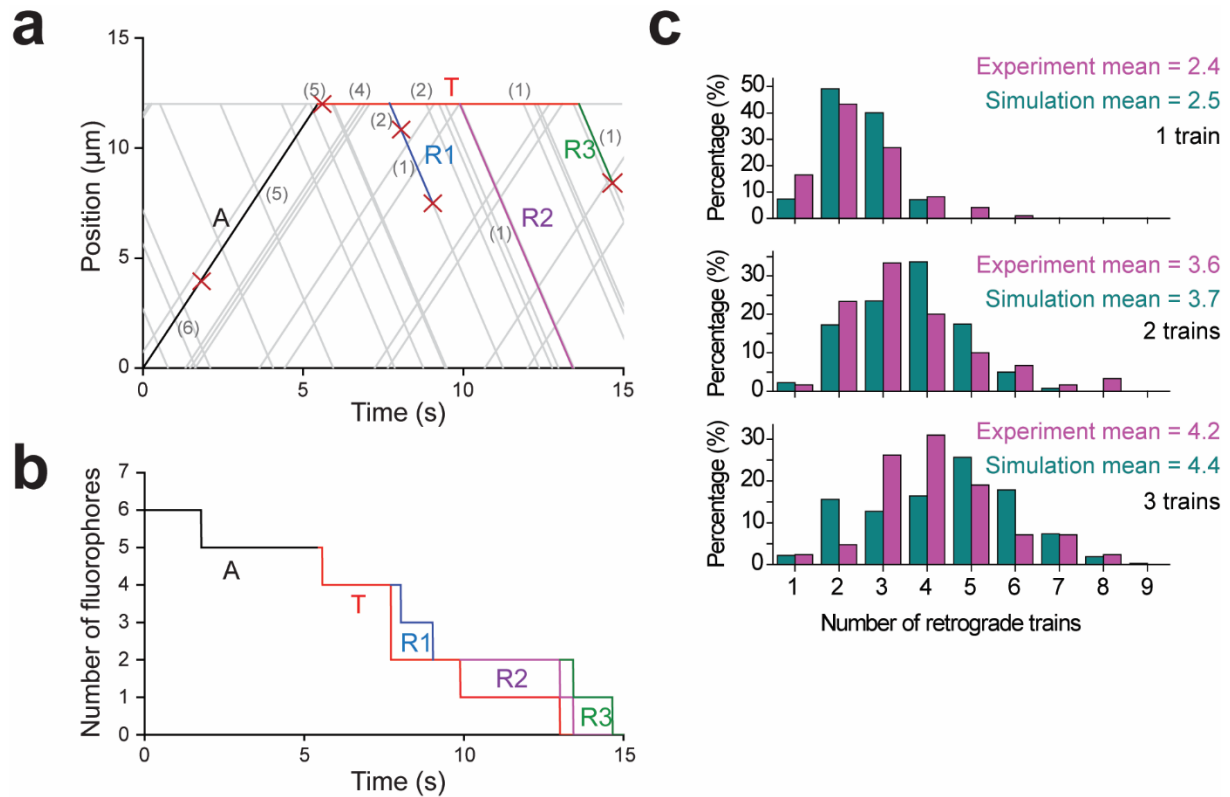


Figure 1-Figure Supplement 3. Monte Carlo simulations for the dynamics of IFT trains at the flagellar tip.

(a) A simulated kymograph with one anterograde IFT train (label A, black line) reaching the flagellar tip, joining the pool at the tip (label T, red line), and returning as three retrograde IFT trains (label R1-R3; blue, purple, and green lines). The anterograde train originally carries 6 bright fluorophores, and each fluorophore either bleaches or returns back to the flagellar base. The number of fluorophores is labeled in grey color within parentheses, and each bleaching event is indicated by a red cross. (b) The total number of fluorophores in the anterograde train (label A, black line), at the flagellar tip (label T, red line), and the retrograde trains (label R1-R3, blue line, purple line and green line) are shown as a function of time for the example kymograph shown in (a). Step-by-step reduction in GFP numbers in anterograde and retrograde trains is due to photobleaching of GFPs at 0.07 s^{-1} under TIR illumination. (c) The number of detectable

991 retrograde trains in PhotoGate assays with one, two, and three fluorescent anterograde trains
992 arriving at the tip in experiments (Figure 1f) and Monte Carlo simulations ($N = 10,000$ for
993 simulations).

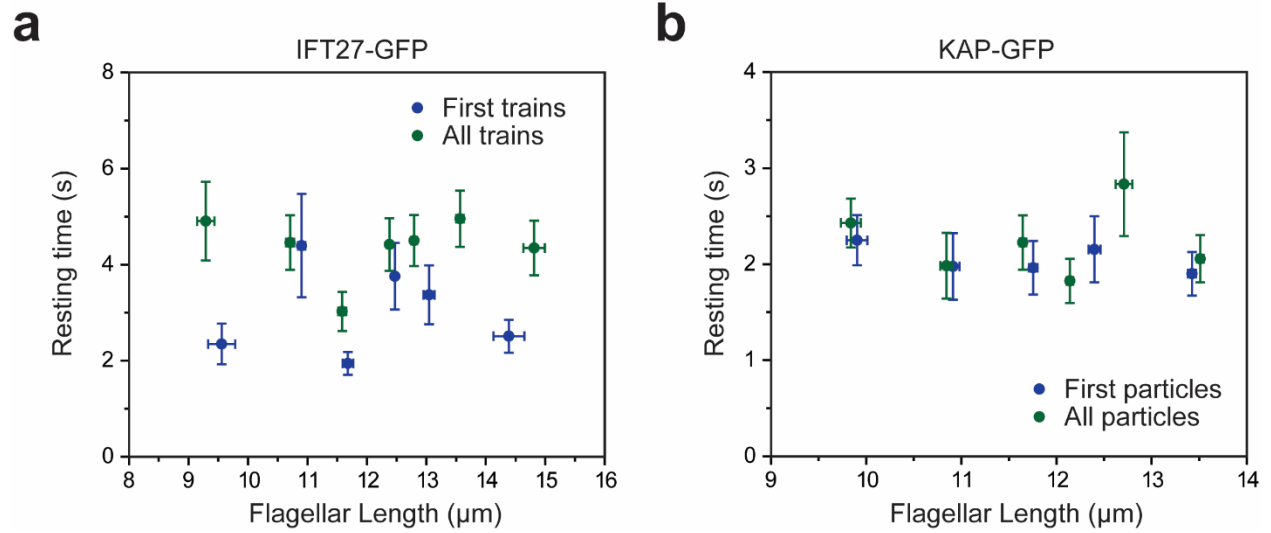
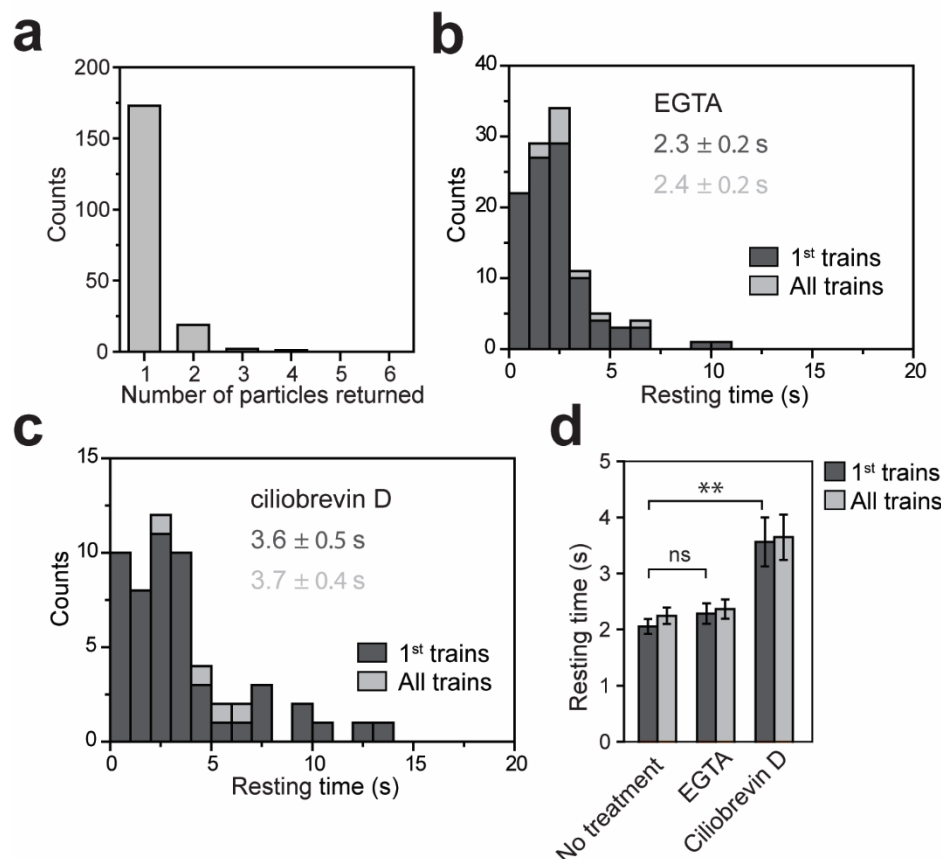


Figure 2-Figure Supplement 1. Tip resting time is independent of flagellar length.

(a,b) The average tip resting time of IFT27-GFP trains (a) and KAP-GFP particles (b) at different lengths of steady-state flagella. Error bars in both axes represent s.e.m. For IFT27-GFP, N = 60 (first train) and 136 (all trains). The bin size is 10 particles. For KAP-GFP, N = 95 (first particle) and 111 (all particles). The bin size is 20 particles.



1000

1001 **Figure 3-Figure Supplement 1. Tip resting time of KAP-GFP under various drug**

1002 **treatments. (a)** The number of fluorescent KAP particles emanating from a single fluorescent

1003 anterograde KAP particle at the tip. N = 195 trains in 106 cells over 9 independent experiments.

1004 All KAP clusters displayed diffusive movement after leaving the tip. **(b)** The tip resting time

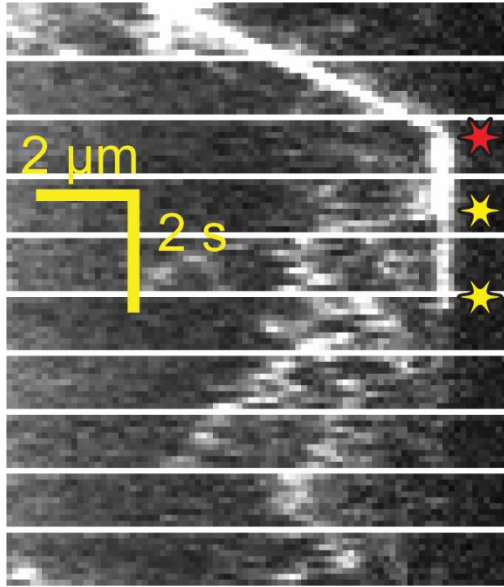
1005 histogram of KAP-GFP with EGTA treatment. N = 100 trains in 59 cells over 5 independent

1006 experiments. **(c)** Tip resting time histogram of KAP-GFP with ciliobrevin D treatment. N = 52

1007 trains in 37 cells over 4 independent experiments. **(d)** The average tip resting time for KAP-GFP

1008 under EGTA and ciliobrevin D treatments (mean \pm s.e.m.; **p < 0.01 as compared to no

1009 treatment; ns is non-significant).



1010

1011 **Figure 3-Figure Supplement 2. Example kymograph of KAP particle breaking apart after**
 1012 **tip departure.**

1013 Kinesin moves anterograde trains to the flagellar tip, dissociates from the IFT trains at the tip,
 1014 and diffuses within the flagellum. In this example, the KAP particle breaks apart into smaller
 1015 particles while diffusing. Red and yellow stars indicate arrival to and departure from the tip,
 1016 respectively.

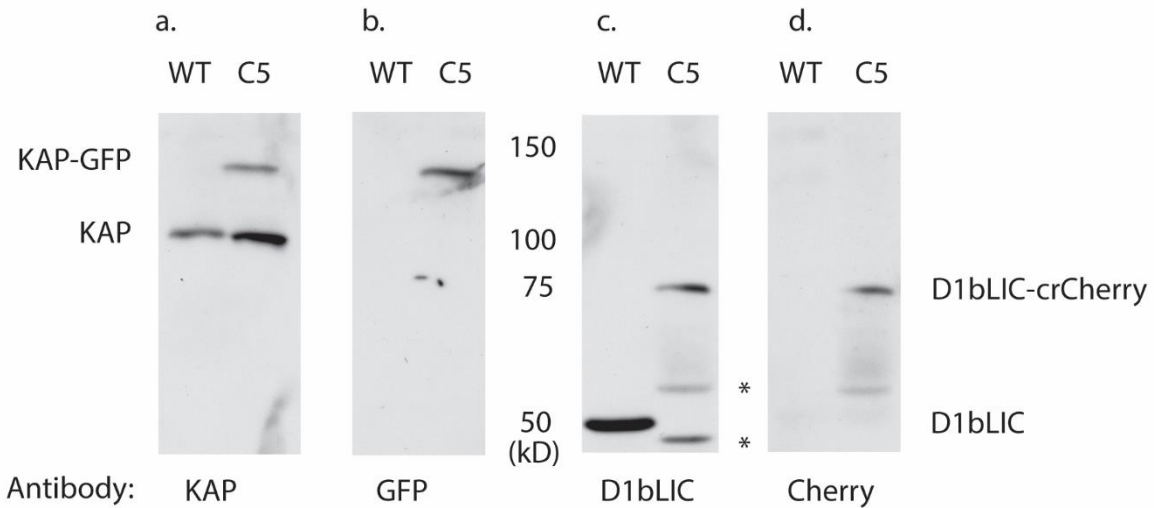


Figure 4-Figure Supplement 1. Expression of KAP-GFP and D1bLIC-crCherry in isolated flagella from a double-tagged strain.

Isolated flagella from wild-type cells (WT) and a *d1blic::D1bLIC-crCherry KAP-GFP* strain (C5) were analyzed on Western blots probed with antibodies against (a) KAP, (b) GFP, (c) D1bLIC, and (d) Cherry. The endogenous KAP subunit migrates at ~95 kD in both strains (a), and the KAP-GFP subunit migrates at ~122 kD (a, b). The D1bLIC subunit migrates at ~49 kD in WT (c) and the D1bLIC-crCherry migrates at ~75 kD in the C5 rescued strain (c, d). The lower molecular weight bands in the C5 rescued strain represent proteolytic fragments of the D1bLIC-crCherry polypeptide (black asterisks). These bands are variable in preparations of isolated flagella.

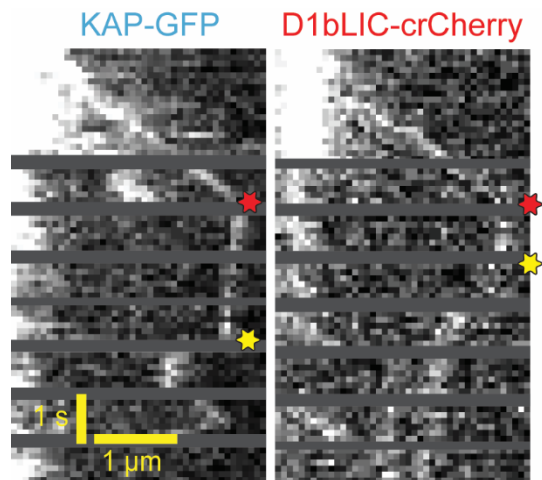
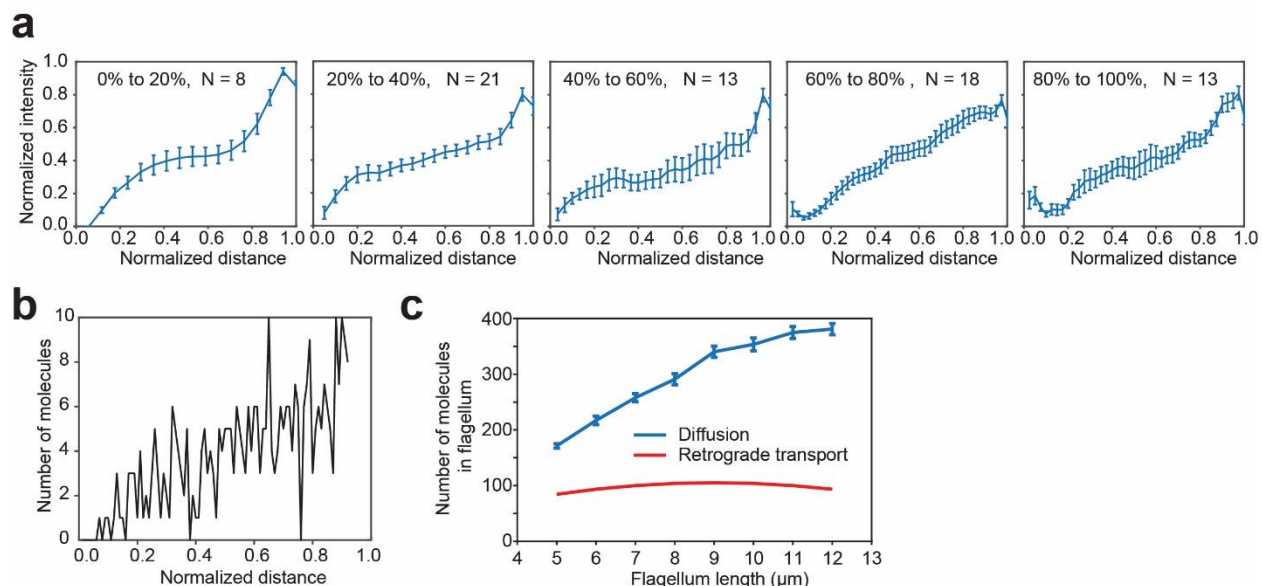


Figure 4-Figure Supplement 2. Example two-color PhotoGate trace of KAP-GFP (left) and D1bLIC-crCherry (right) in single flagella. KAP-GFP and D1bLIC-crCherry arrive at the tip on the same train. In this example, D1bLIC leaves the tip before KAP. Red and yellow stars indicate arrival to and departure from the flagellar tip, respectively.

1033



1034

1035 **Figure 5-Figure Supplement 1. A gradient of KAP-GFP fluorescence along the length of the**
 1036 **flagellum exists across all flagellar lengths.**

1037 **(a)** The gradient of KAP-GFP fluorescence is approximately linear over the length of the
 1038 flagellum for flagella of different lengths. Cells undergoing flagellar regrowth were imaged and
 1039 split into groups by their flagellar length, as a percentage of full-length flagella. IFT trains were
 1040 manually removed from kymographs and remaining pixels were time-averaged to calculate the
 1041 concentration gradient of the KAP-GFP. Error bars represent s.e.m. N = 57 kymographs over 5
 1042 independent experiments. **(b)** Monte Carlo simulations reveal the flagellar distribution of KAP-
 1043 GFP diffusing from a source at the tip (right) to a sink at the base (left). **(c)** Simulations show
 1044 that return of KAP to the cell body by diffusion leads to a greater accumulation of KAP in the
 1045 flagellum, in comparison to a hypothetical case where KAP returns to the cell body via
 1046 retrograde transport. This analysis accounts for both anterogradely moving and diffusing KAP
 1047 molecules.

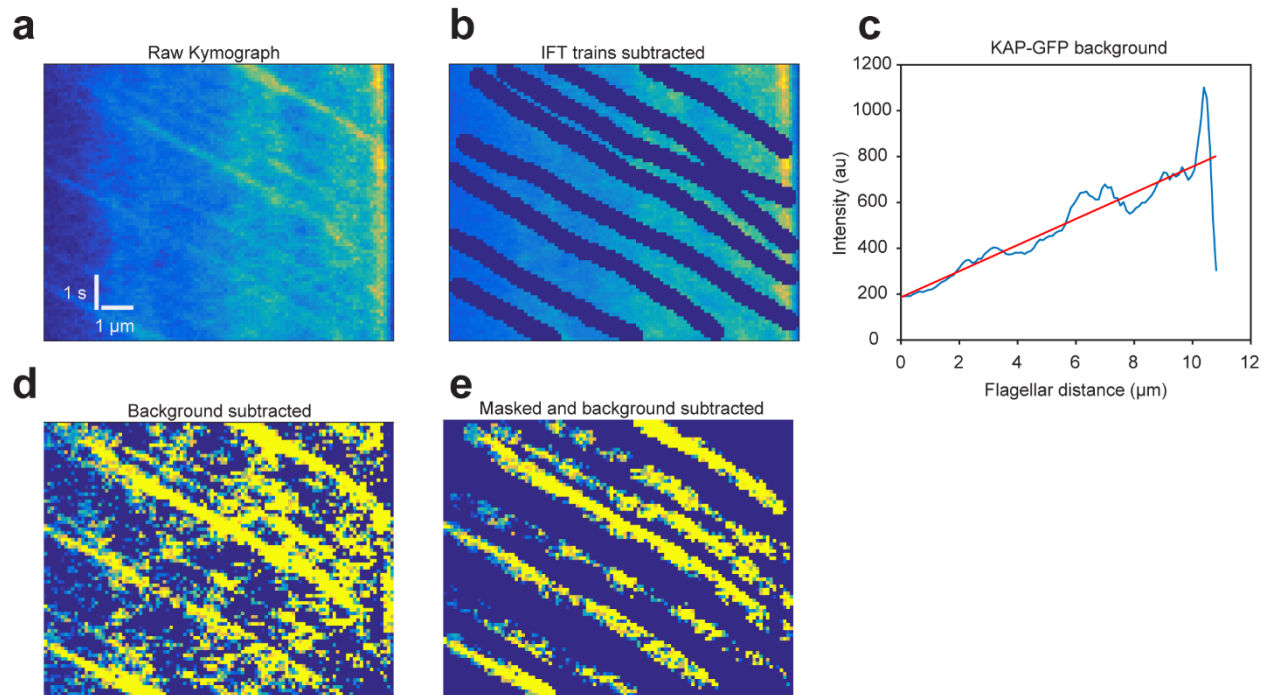


Figure 5-Figure Supplement 2. The influx and efflux of KAP-GFP fluorescence in fully grown flagella are equal.

(a) An example kymograph of a *fla3::KAP-GFP* flagellum imaged with TIR. The flagellar tip is on the right. (b) To calculate the intensity of the fluorescence background, anterograde trajectories of KAP were manually subtracted from the kymograph. (c) Intensities were time-averaged to calculate KAP-GFP background. Efflux was calculated from Fick's law using the slope of the intensity profile along the flagellar length and the measured diffusion constant ($1.7 \mu\text{m}^2 \text{s}^{-1}$). (d) Background was subtracted from original kymograph to get anterograde train intensities. (e) The kymograph was masked for anterograde trains to calculate the average fluorescent counts per train. Influx was calculated by multiplying counts per train with the measured train frequency (1.3s^{-1}). KAP-GFP influx into the flagellum ($1,130 \pm 70 \text{ counts s}^{-1}$) was similar to the efflux of KAP from the flagellum ($1,170 \pm 160 \text{ counts s}^{-1}$). $N = 57$ kymographs over 5 independent experiments (mean \pm s.e.m.).

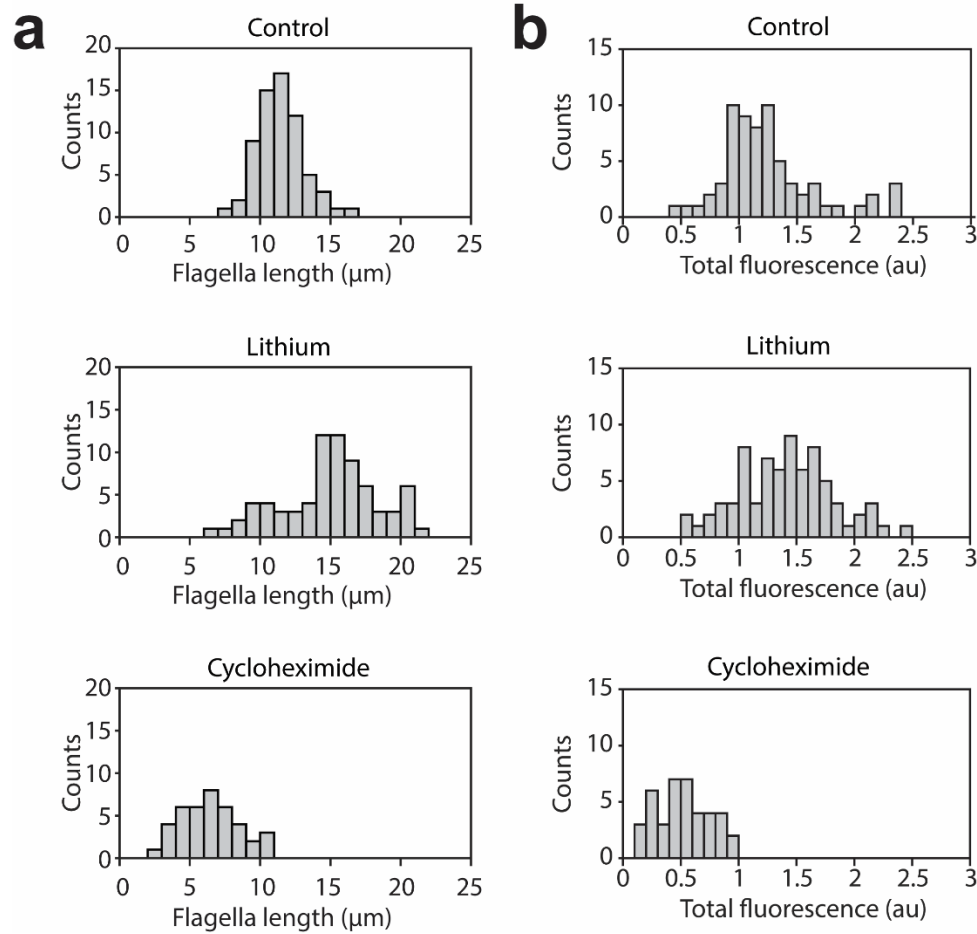


Figure 6-Figure Supplement 1. Length and total fluorescence distributions of lithium and cycloheximide-treated cells.

(a) Flagella length distributions for *fla3::KAP-GFP* cells cultured in TAP media, cells treated with 50 mM LiCl, and cells subjected to pH shock and allowed to regrow flagella in the presence of 1.5 ug/ml cycloheximide. For control cells, N = 66 flagella from 33 cells. For lithium-treated cells, N = 74 flagella from 37 cells. For cycloheximide-treated cells, N = 40 flagella from 20 cells. **(b)** Histograms show the total fluorescent signal of KAP-GFP localized to the basal body and the flagellum of single cells.

2. Video Legends

Video 1. Tracking of individual IFT trains in *Chlamydomonas*. IFT movement was visualized by TIR imaging of a surface-adhered *pf18 IFT27-GFP* cell. Green and blue arrows represent the cell body and flagellar tips, respectively. The size of the window is $15.5 \times 27.6 \mu\text{m}$. The movie was recorded at 10 frames s^{-1} and is played in real time. This video corresponds to Figure 1a.

Video 2. Observing the dynamics of single IFT trains at the flagellar tip using the PhotoGate. The distal half of the flagellum on the right of a surface-adhered *pf18 IFT27-GFP* cell is photobleached by an intense laser beam. The gate beam is turned off to allow a single anterograde train to enter the bleached region and turned on repeatedly at the base of the flagellum to bleach the subsequent anterograde trains. Two retrograde trains emanate from a single fluorescent anterograde train at the tip. Frames with the gate beam on are removed for illustration purposes. The movie was recorded at 10 frames s^{-1} and is played in real time. Cyan and magenta arrows represent anterograde and retrograde particles, respectively. Pre-bleaching frames are marked by red borders. The position of the PhotoGate is marked by a red line. This video corresponds to Figure 1c.

Video 3. Tip return dynamics of two fluorescent anterograde trains using the PhotoGate. A flagellum of a surface-adhered *pf18 IFT27-GFP* cell is photobleached. Two fluorescent anterograde IFT trains are allowed pass through the gate without photobleaching and subsequent anterograde trains were photobleached by the gate beam. After the anterograde trains reach the tip, three retrograde trains return with fluorescent signal from these trains. The movie was recorded at 10 frames s^{-1} and is played in real time. Cyan and magenta arrows represent anterograde and retrograde particles, respectively. The position of the PhotoGate is marked by a red line. This video corresponds to Figure 1d.

1094 **Video 4. Tip return dynamics of three fluorescent anterograde trains using the PhotoGate.**

1095 A flagellum of a surface-adhered *pf18 IFT27-GFP* cell is photobleached. Three fluorescent
1096 anterograde IFT trains are allowed pass through the gate without photobleaching and subsequent
1097 anterograde trains were photobleached by the gate beam. The frames in which the gate beam was
1098 on were deleted for illustration purposes. After the anterograde trains reach the tip, four
1099 retrograde trains return with fluorescent signal from these trains. The movie was recorded at 10
1100 frames s^{-1} and is played in real time. Cyan and magenta arrows represent anterograde and
1101 retrograde particles, respectively. Pre-bleaching frames are marked by red borders. The position
1102 of the PhotoGate is marked by a red line. This video corresponds to Figure 1e.

1103 **Video 5. Tip return dynamics of D1bLIC-GFP.** In a surface-adhered *d1blic::D1bLIC-GFP*

1104 cell, one D1bLIC-GFP particle is allowed to pass through the gate without photobleaching and
1105 two fluorescent retrograde particles return to the base. The movie was recorded at 10 frames s^{-1}
1106 and is played in real time. Cyan and magenta arrows represent anterograde and retrograde
1107 particles, respectively. Pre-bleaching frames are marked by red borders. The position of the
1108 PhotoGate is marked by a red line. This video corresponds to Figure 3c.

1109 **Video 6. KAP-GFP dissociates from IFT trains at the tip.** In the *fla3::KAP-GFP* strain, one

1110 fluorescent KAP-GFP particle is allowed to pass through the gate without photobleaching. The
1111 KAP-GFP particle undergoes diffusive motion after arriving at the flagellar tip. The size of the
1112 window is $26.6 \times 16.6 \mu m$. The movie was recorded at 10 frames s^{-1} and is played in real time.
1113 Cyan and magenta arrows represent anterograde and diffusing particles, respectively. The
1114 position of the PhotoGate is marked by a red line. This video corresponds to Figure 3f.

1115 **Video 7. Diffusing KAP-GFP particles can break apart after leaving the tip.** In the

1116 *fla3::KAP-GFP* strain, one fluorescent KAP-GFP particle is allowed to pass through the gate

1117 without photobleaching. The KAP-GFP particle undergoes diffusive motion after arriving at the
1118 flagellar tip. While diffusing, the particle breaks further into smaller KAP particles. The size of
1119 the window is $30.2 \times 31.1 \mu\text{m}$. The movie was recorded at 10 frames s^{-1} and is played in real
1120 time. Cyan and magenta arrows represent anterograde and diffusing particles, respectively. The
1121 position of the PhotoGate is marked by a red line. This video corresponds to Figure 3-
1122 supplementary figure 2.

1123 **Video 8. Dual color imaging of KAP-GFP and D1bLIC-crCherry.** The movements of KAP-
1124 GFP and D1bLIC-crCherry are simultaneously tracked in a surface-adhered *d1blic::D1bLIC-*
1125 *crCherry KAP-GFP* cell. KAP and D1bLIC co-localize in the anterograde direction. D1bLIC
1126 displays retrograde tracks while retrograde transport of KAP is rarely seen. KAP-GFP channel is
1127 on the left and D1bLIC-crCherry channel is on the right. The movie was recorded at $8.3 \text{ frames s}^{-1}$
1128 and is played in real time. This video corresponds to Figure 4a.

1129 **Video 9. Recovery of KAP-GFP after photobleaching the middle section of a flagellum.** A
1130 surface-adhered *fla3::KAP-GFP* is imaged under TIRF illumination. The middle part of the
1131 flagellum is bleached by a 25 kW cm^{-2} laser beam for 0.1 s and the cell is imaged under 100 W
1132 cm^{-2} TIRF excitation. The fluorescent signal recovers with different kinetics from each side of
1133 the flagellum. The data was collected at 10 frames s^{-1} and is played in real time. Green and blue
1134 arrows represent the cell body and flagellar tips, respectively. The photobleached area is marked
1135 by thin red lines. This video corresponds to Figure 5a.

Figure 1

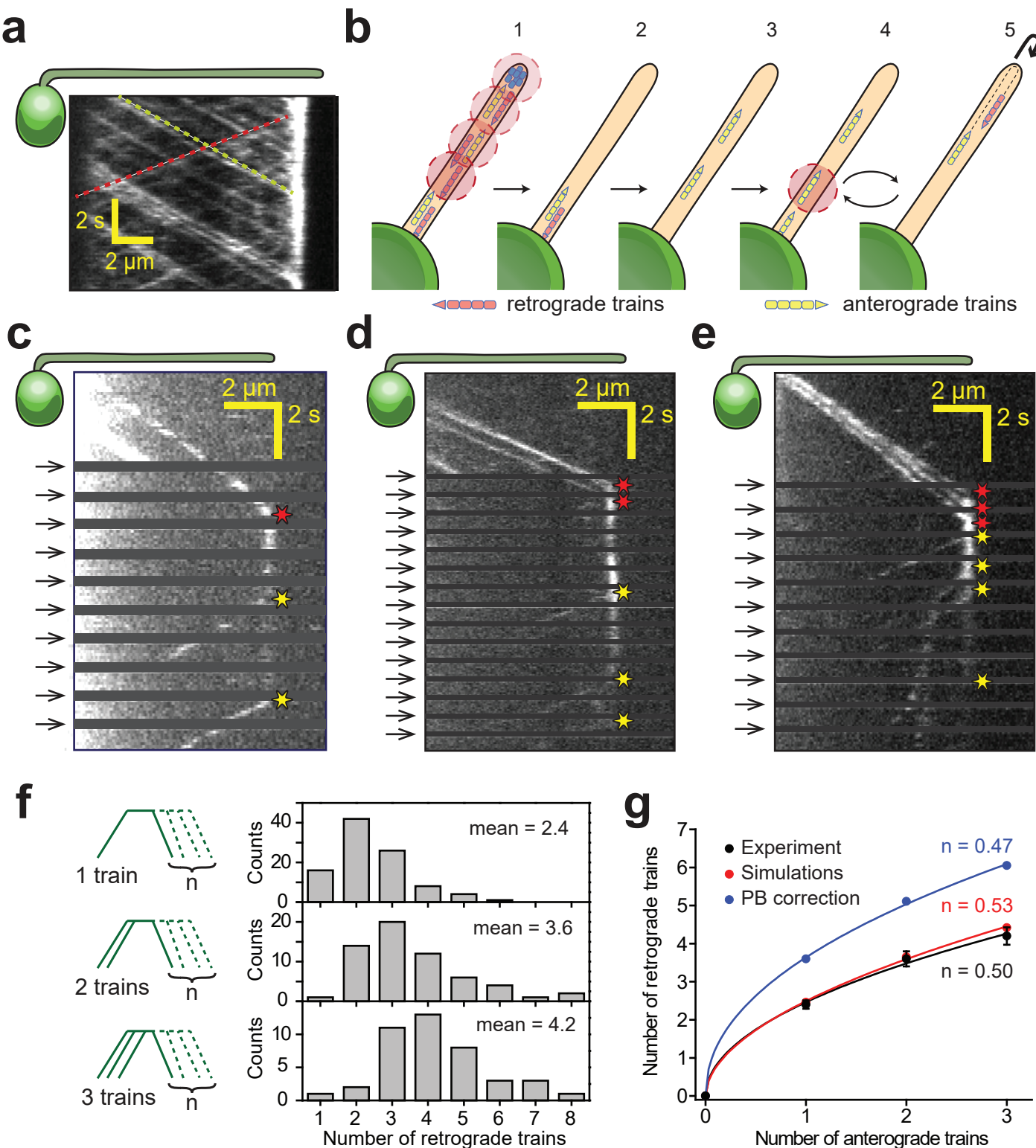


Figure 2

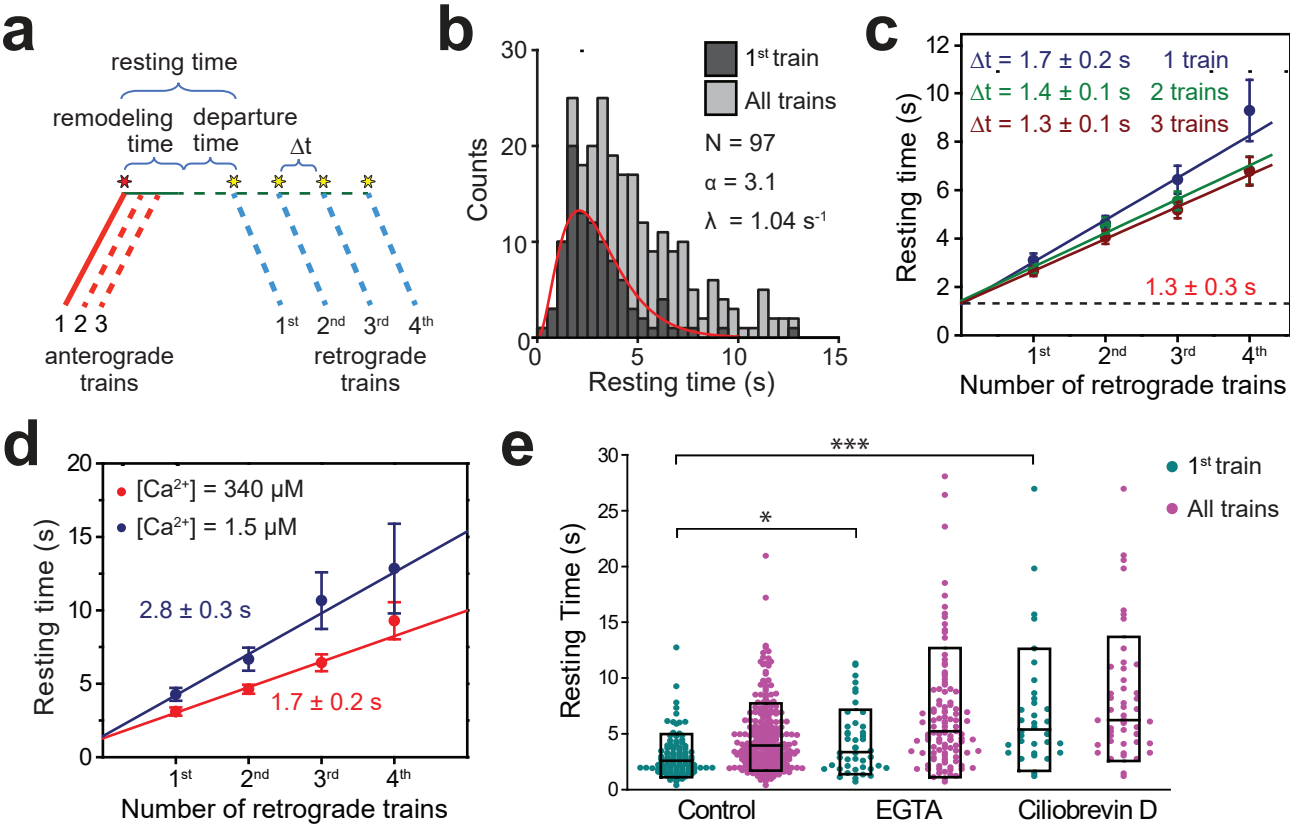


Figure 3

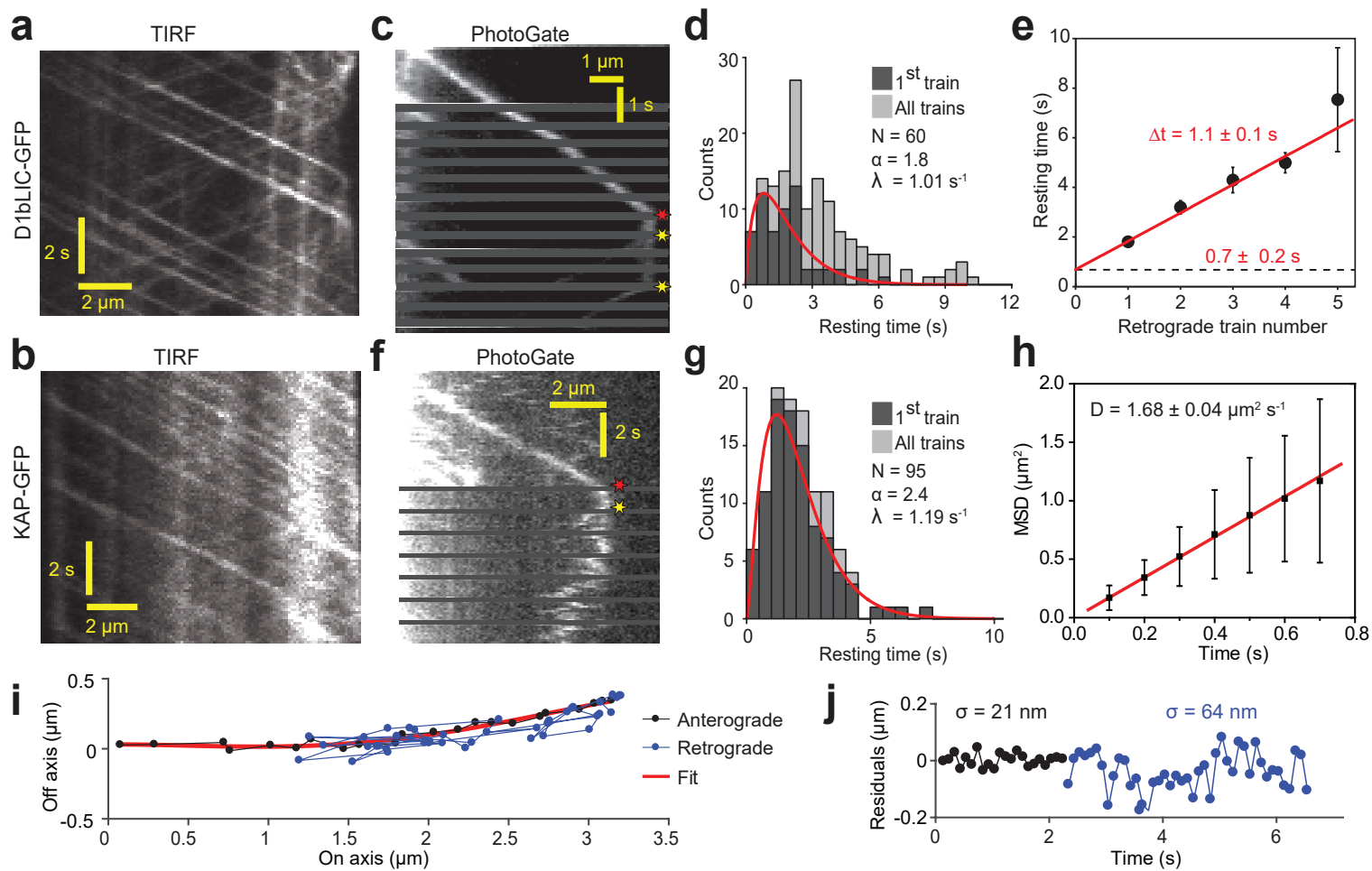


Figure 4

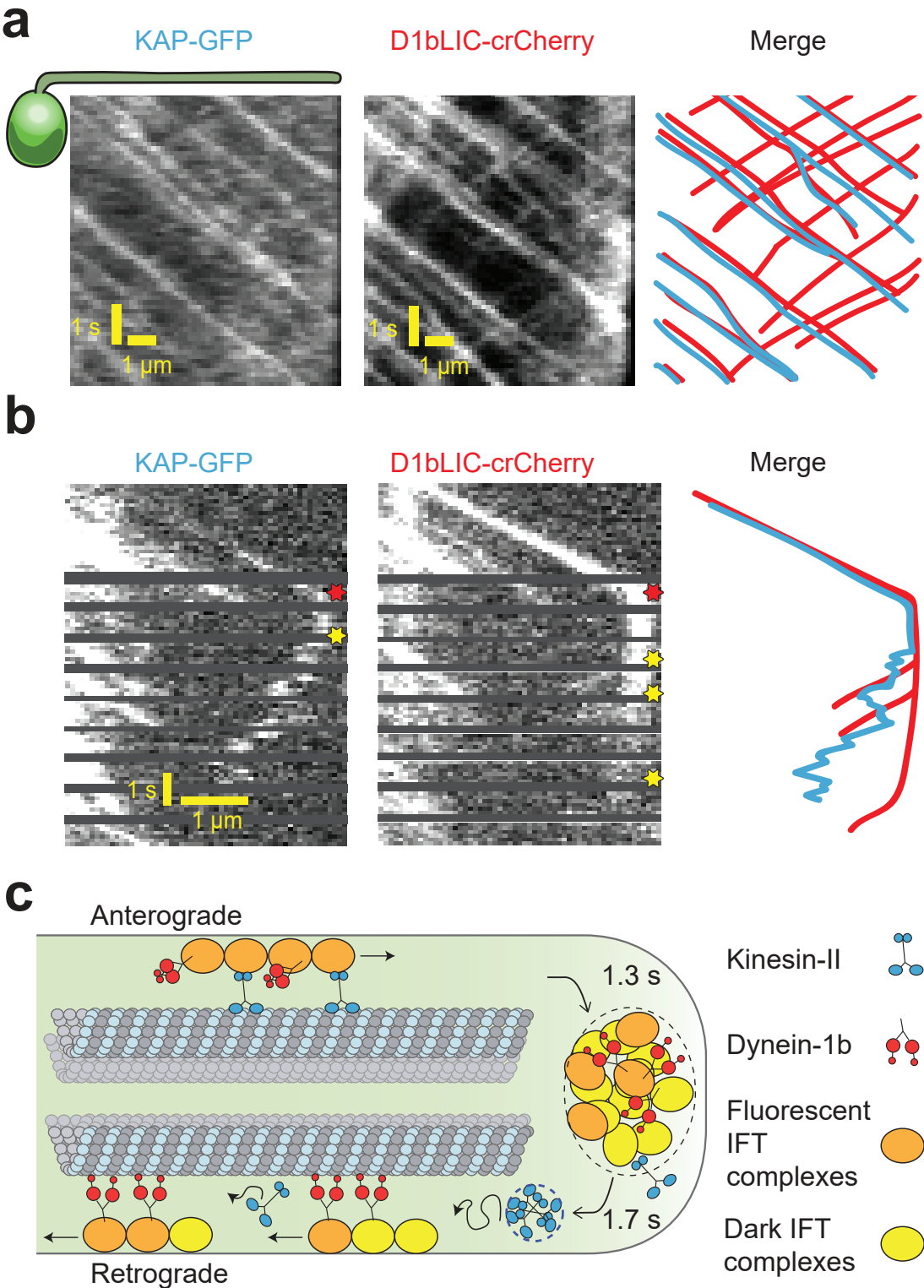


Figure 5

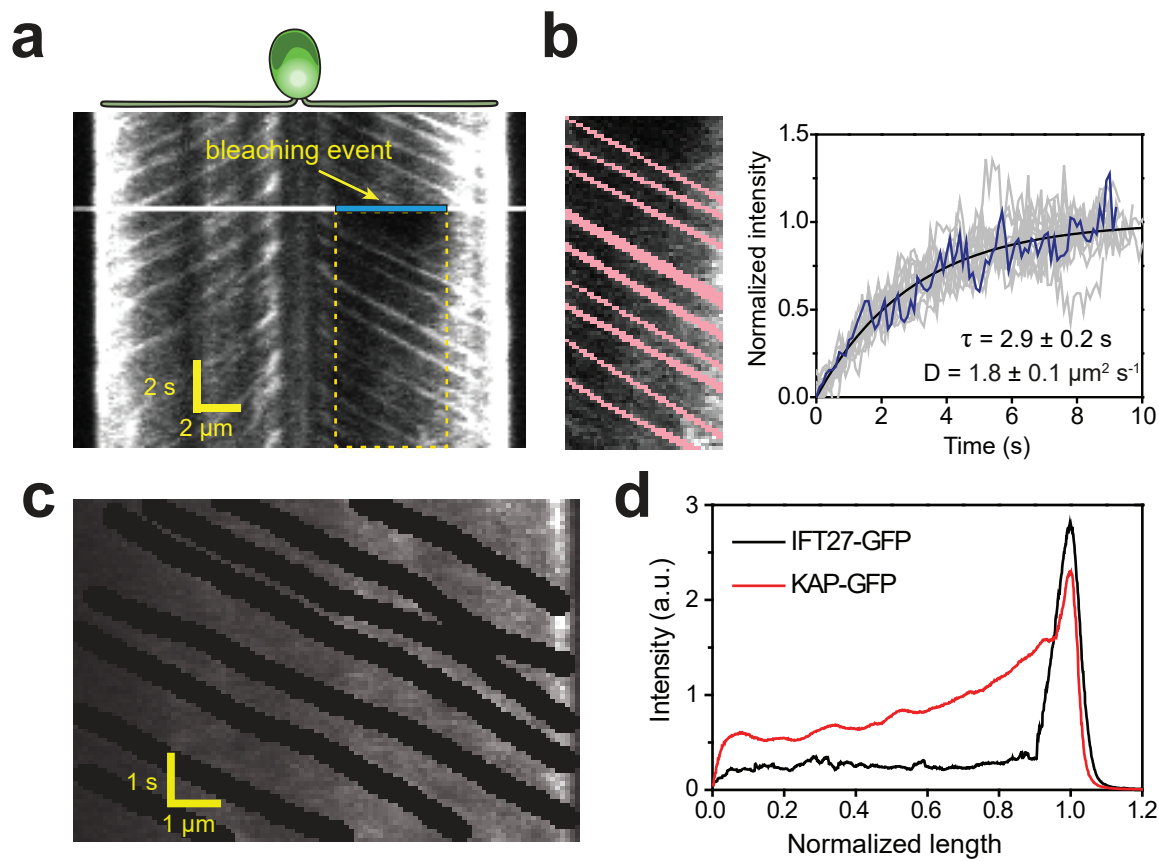
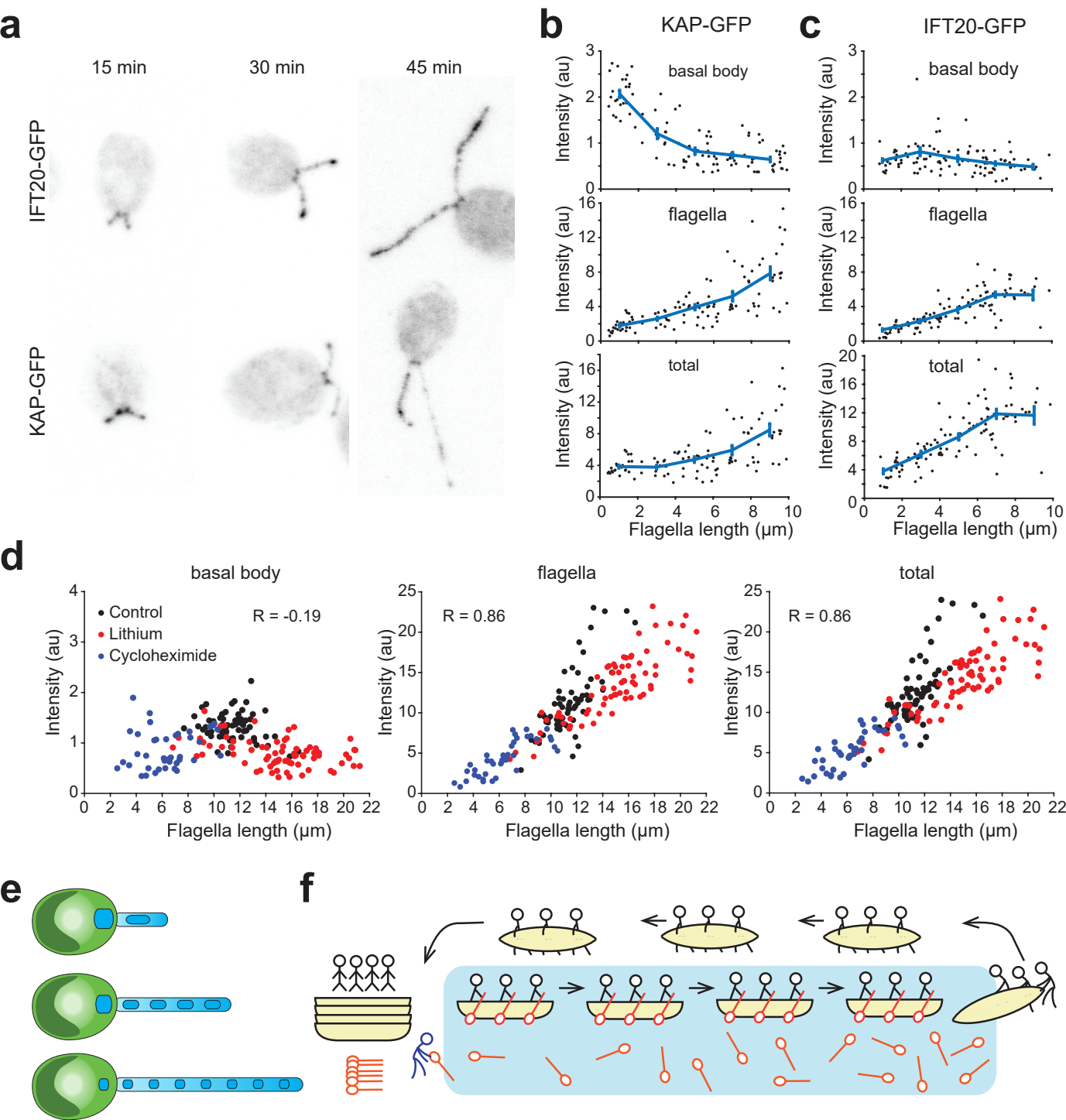
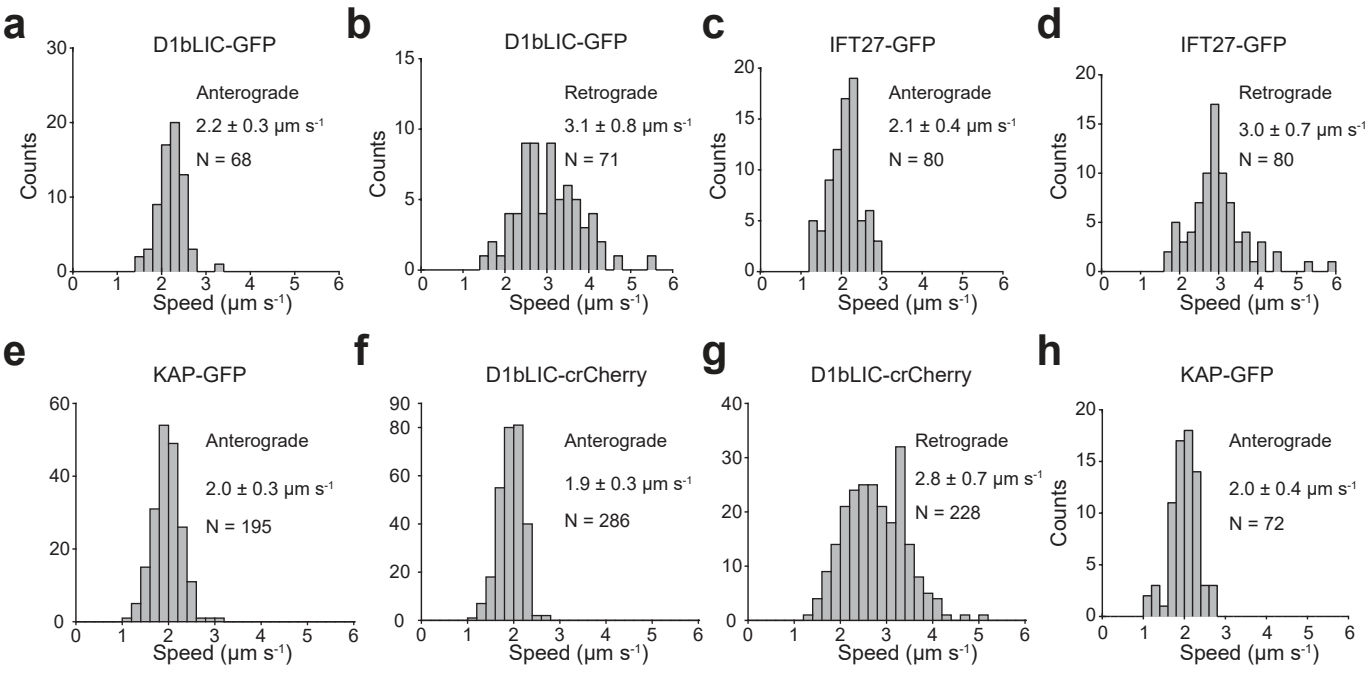


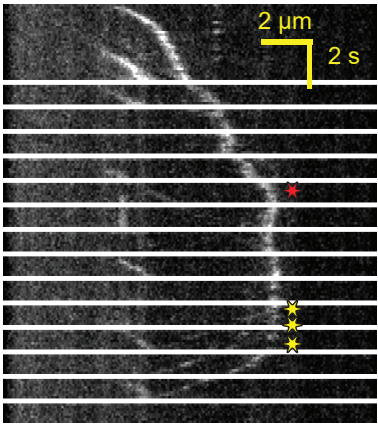
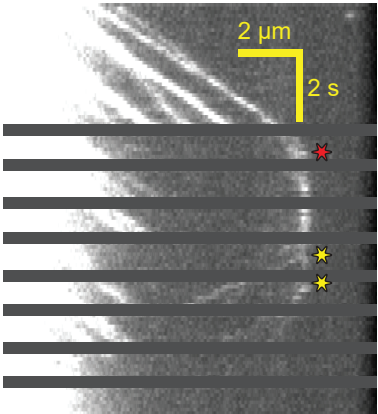
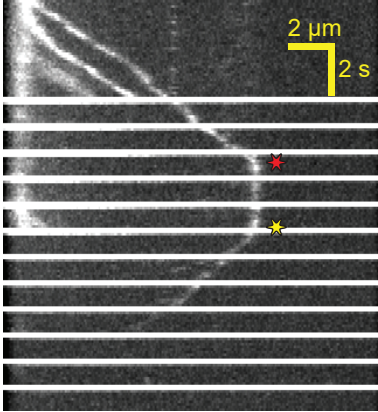
Figure 6





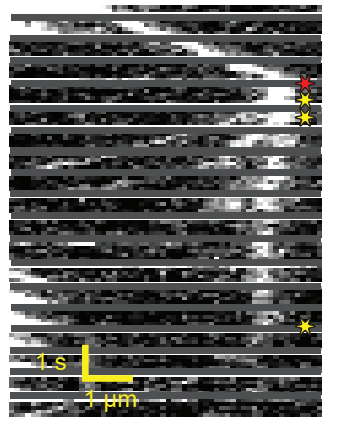
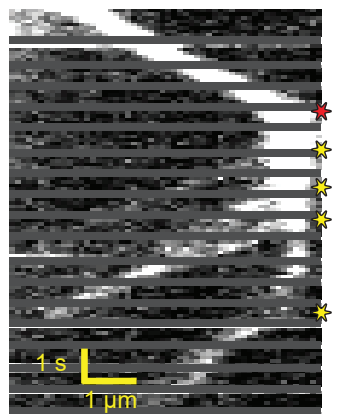
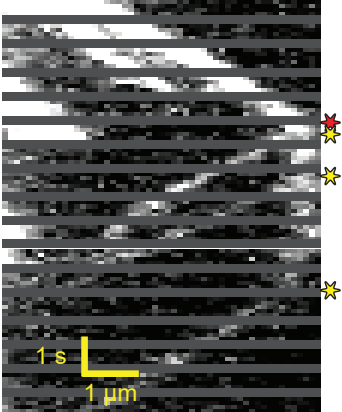
a

IFT27-GFP



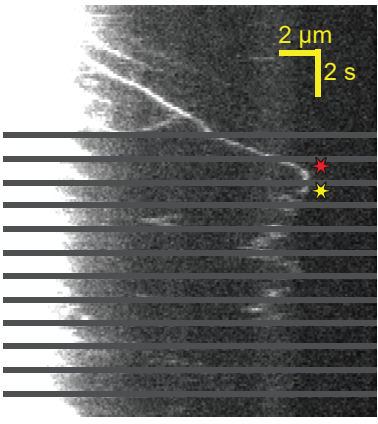
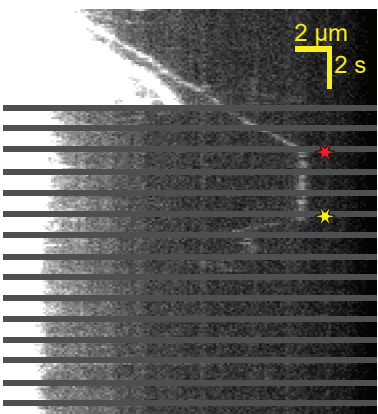
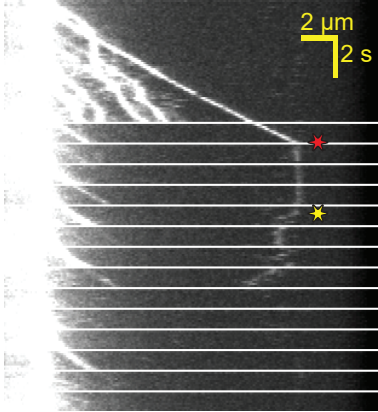
b

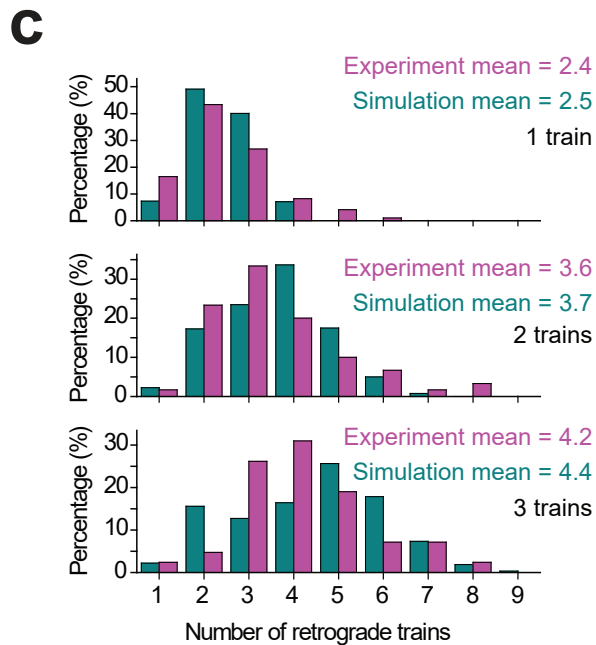
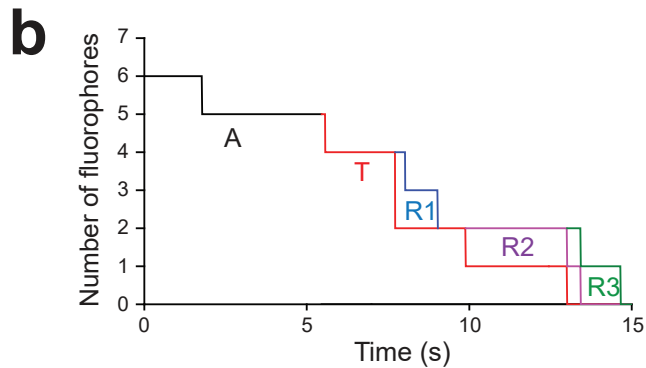
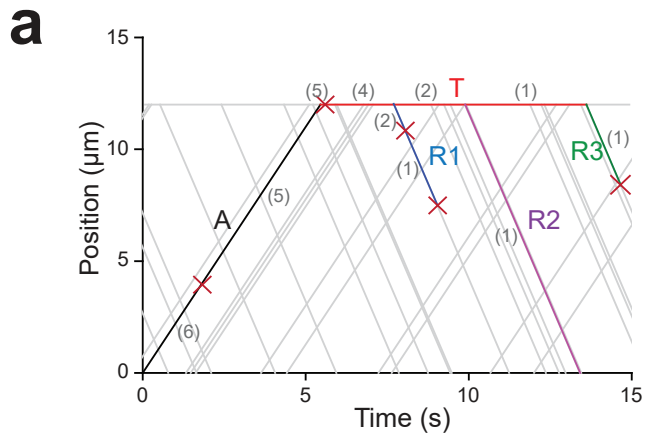
D1bLIC-GFP

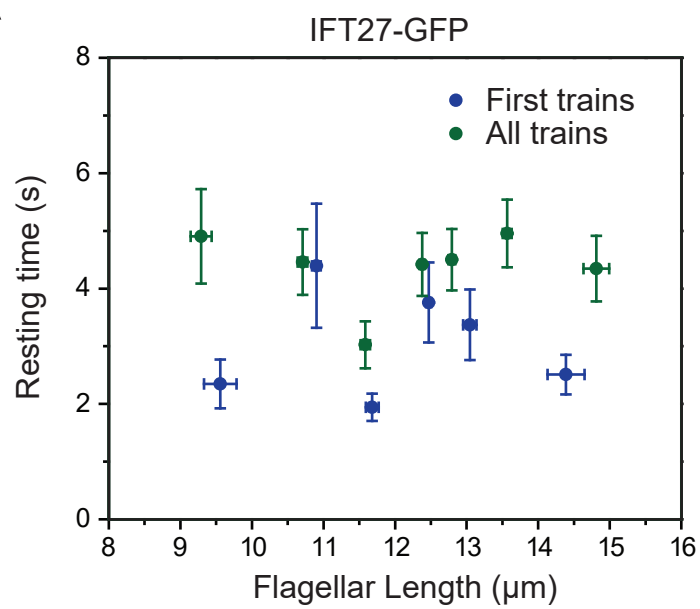
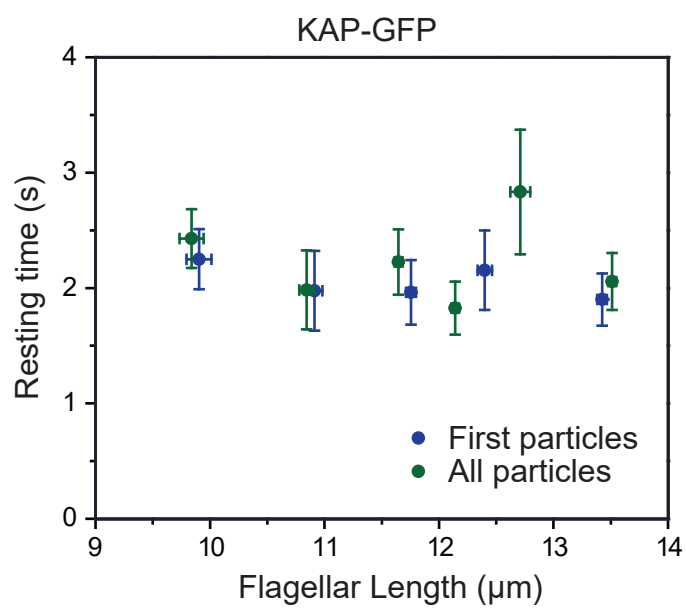


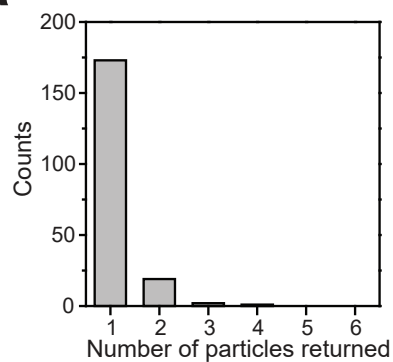
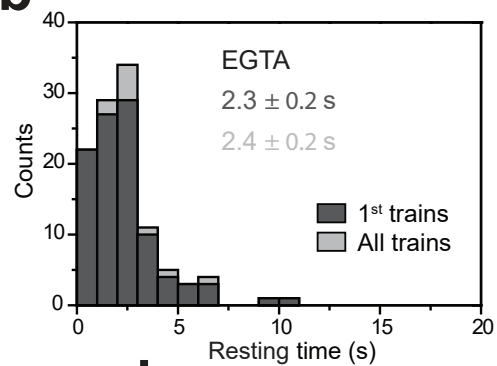
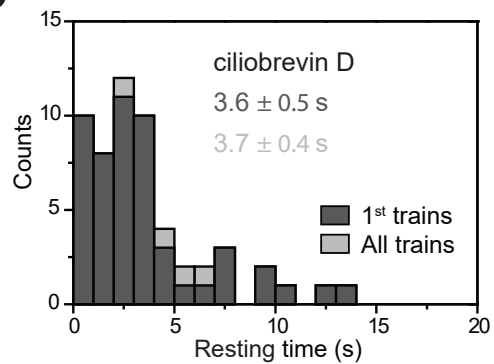
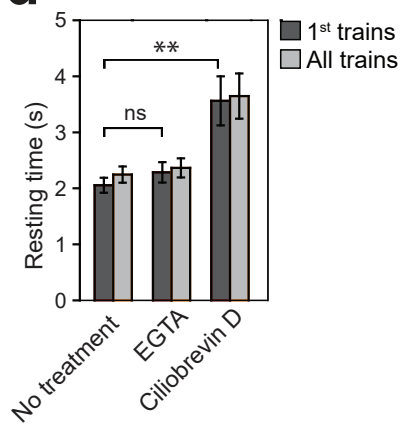
c

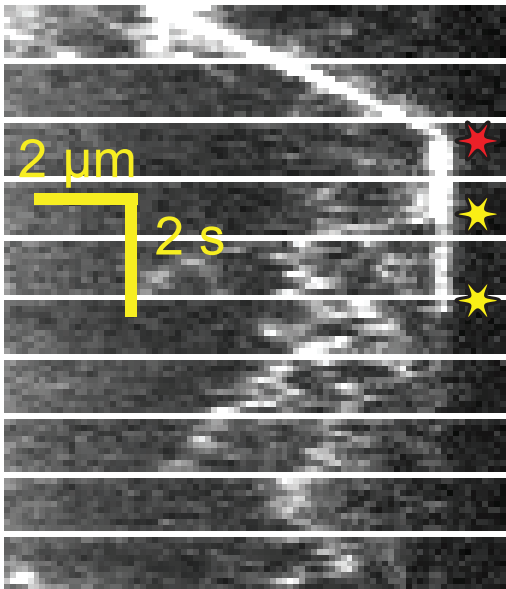
KAP-GFP

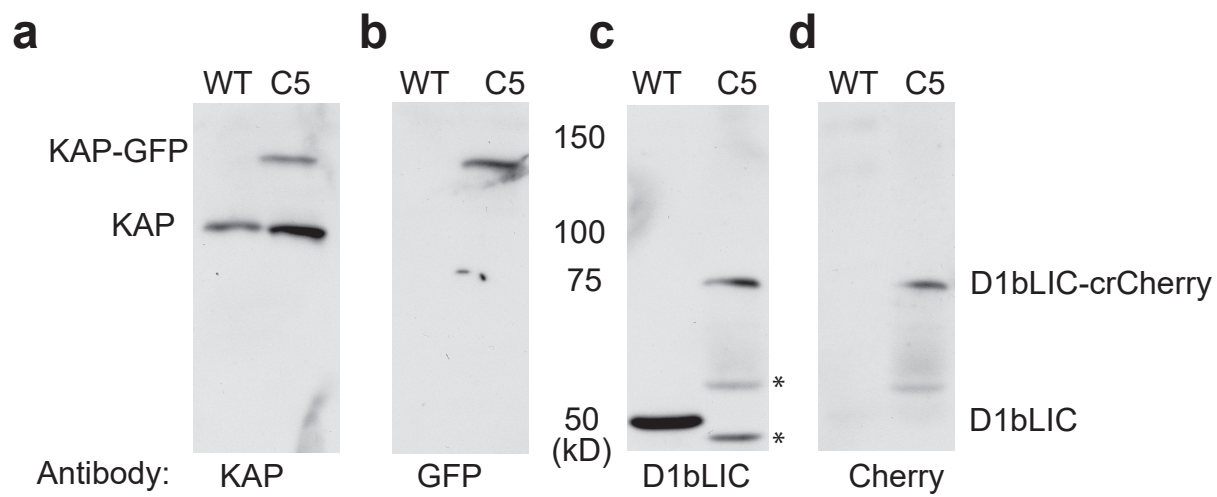


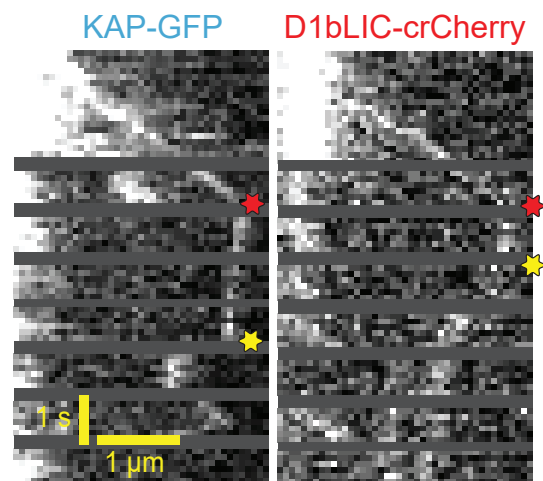


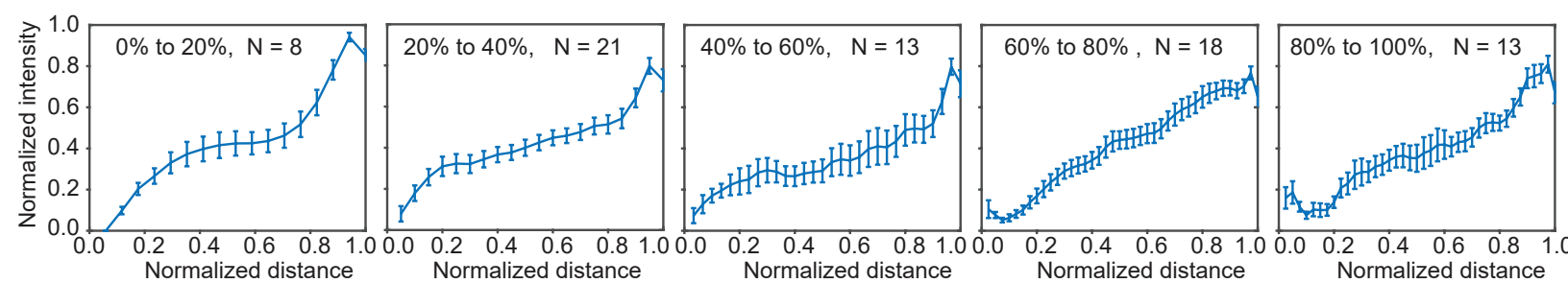
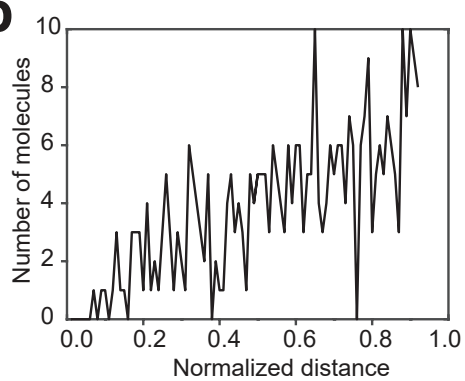
a**b**

a**b****c****d**







a**b****c**